Geometric Constraints for the Cascadia Subduction Zone Beneath Indian Island, Washington from Teleseismic Receiver Function Analysis

by

Kimberley Marie Edlund

A thesis submitted in partial fulfillment
of the requirements for the degree of

Master of Science

University of Washington

1991

Approved by Robert L Preston
(Chairperson of Supervisory Committee)

Program Authorized
to Offer Degree Geophysics Program

Date August 12, 1991

Master's Thesis

In presenting this thesis in partial fulfillment of the requirements for a Master's degree at the University of Washington, I agree that the Library shall make its copies freely available for inspection. I further agree that extensive copying of this thesis is allowable only for scholarly purposes, consistent with "fair use" as prescribed in the U.S. Copyright Law. Any other reproduction for any purposes or by any means shall not be allowed without my written permission.

Signature Kim Edlund

Date 12 August 1991

Table of Contents

List of Figures

List of Tables

Acknowledgements

I gratefully acknowledge the contributions made to this work. Many people made this study possible through previous research in the region, site selection and trouble-shooting, equipment maintenance, data collection, discussions, helpful suggestions, and the development of working programs and workable procedures: Robert Crosson; my friend, Ruth Ludwin; Laurens Engel; Ken Creager; Tom Owens; and Lee Bond. Thanks to the reviewers of this manuscript who were very generous with their time and patience.

I am grateful for the many friends who encouraged me: G.W. Gross, D.A. Crain, Kathy Sharpe, Kevin Crain, Jb Eriksen, as well as countless others. John VanDecar was an interesting and challenging office mate and friend, and introduced me to the evils of PostScript.

I was supported financially by a National Science Foundation Graduate Student Fellowship and by a Dorothy Danforth-Compton Graduate Student Fellowship, and I owe special thanks to all the 'Compton folks at UW.

Most especially and with deep affection, I wish to thank Greg Titus, Juhli Alden, Brian Smith, and Jeff Musiak for their constant support and love, and for always being there when my wheels fell off.

Dedication

This work is dedicated with appreciation, love, and hope to Uncle Bud and Aunt Katie, and the Grandmothers.

"Listen, my sons! Listen to a song for life,
The words are good. The song is old.
Hear me now! Inside each of you, there
belts a drum. Drums that are never silent...

I wish that your grandmothers could see
you now. I wish they could reach out and
touch you. For they were the ones who
gave their drums to you."

-Anna Lee Walters [1975]

Chapter 1

Introduction

The dramatic geology and topography of western Washington is dominated by the influence of the Juan de Fuca (JDF) plate system. Over the last half million years, the JDF plate has been actively converging with the North America plate at an average rate of 3-4 centimeters per year [*Riddihough*, 1984]. The interaction of the two plates is responsible for the Cascade strato-volcanos, the impressive vertical relief of the Olympic Mountains, and the westward accretionary growth of the North American continent. Figure 1.1 shows the regional plate relationships of the present-day system.

Subduction zones are usually seismically active regions and are associated with the largest earthquakes on earth. The Cascadia subduction zone (CSZ) has been the focus of much recent attention in connection with the possibility of large subduction earthquakes [*Heaton* 1990]. *Heaton and Hartzell* [1987] conclude that very strong similarities exist between the CSZ and other subduction zones that have experienced large shallow earthquakes and that the CSZ may be locked, with slip occurring only during infrequent large earthquakes. However, during the last 150 years of written history there has been a lack of documented thrust-type subduction earthquakes at all energy levels.

Discoveries of buried, intertidal marsh surfaces in the coastal low-lands in westernmost Washington state by *Atwater* [1987] suggest that rapid coastal subsidence of the type commonly accompanying great subduction earthquakes has occurred at least six times during the last 7000 years. Anomalous sheets of sand atop at least three of the surfaces suggest that tsunamis could be associated with the same events that caused the subsidence [*Atwater* 1987]. Traditional Makah Indian legends of tsunamis and crustal uplift, possibly associated with local subduction earthquakes, have been reported by *Swann* [1868]. *Heaton and Snavely* [1985] conclude these reports are noteworthy as they exist for a region for which there is growing concern that large subduction earthquakes may be a real possibility.

To properly evaluate the potential hazards associated with this area, knowledge of the geometry of the subducted slab is essential. The structural relationship of the plates that make up this system exerts an important influence on the tectonics and

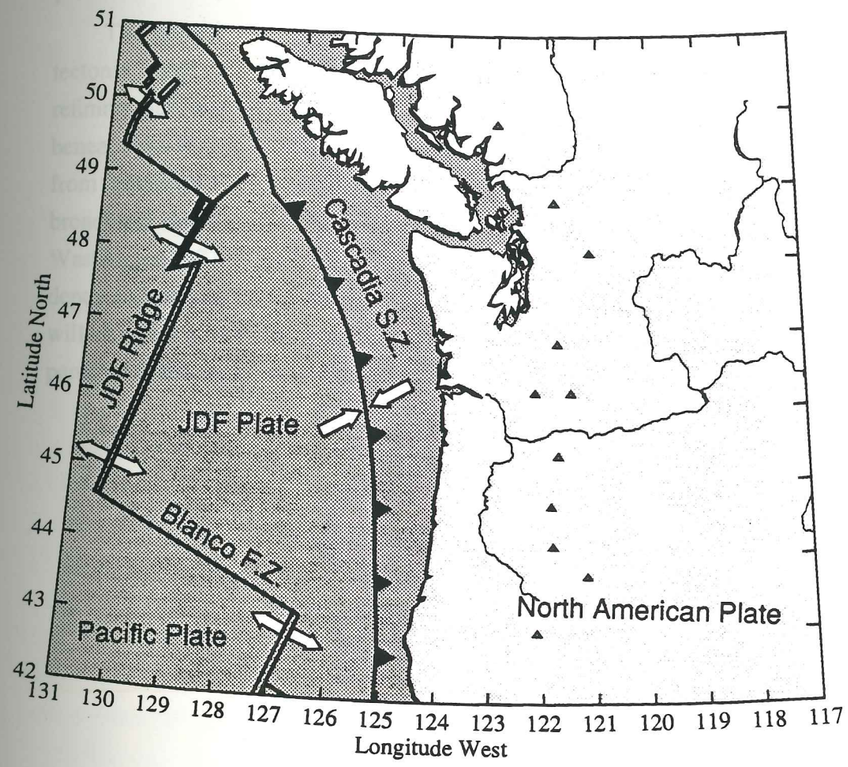

Figure 1.1 Lambert conformal projection of the tectonic structure of the Juan de Fuca plate system and Cascadia subduction zone. Arrows indicate direction of current relative motion along plate boundaries. Triangles are locations of Quaternary strato-volcanos. JDF = Juan de Fuca, F.Z. = fracture zone, and S.Z. = subduction zone.

earthquake generating processes. Studies of interplate and intraplate earthquakes, analyses of regional stress and strain, and investigations of large scale tectonic processes all require accurate models of the plate structure.

The objective of this study is to aid in the fundamental understanding of the tectonic framework, seismicity, and earthquake hazards associated with the CSZ by refining our understanding of the crustal structure and shape of the JDF plate beneath western Washington. To fulfill this objective, receiver functions obtained from teleseismic P-waveforms will be modeled using data collected at a single broadband station deployed at a site on Indian Island, 35 miles northwest of Seattle, Washington. This analysis will provide important geometric constraints on the depth and orientation of the subducted slab immediately beneath Puget Sound. We will develop a velocity structure model of the subducted slab which can be compared with the regional working models.

Chapter 2

Tectonic Framework of the Cascadia Subduction Zone

The tectonic framework of the Cascadia subduction zone has been of interest to earth scientists since the earliest days of plate tectonic theory and the structure of the crust and upper mantle have been investigated using a variety of techniques.

One of the first attempts to describe the geometry of the JDF plate was made by *Dickinson* [1970]. He estimated the approximate depth to the subducted plate using petrologic variations within the andesitic suites of the Cascade volcanic chain. His inferred depth contours suggest an arch in the JDF plate at depth.

Using local hypocenter data and receiver function analysis, *Crosson and Owens* [1987] proposed that the subducted part of the Juan de Fuca plate is arched upward with its axis trending roughly east-west beneath the Olympic Mountains - Puget Sound Region. *Weaver and Baker* [1988], using seismicity data, also illustrated a similar geometry. Figure 2.1 shows the local tectonic framework and depth contours of the subducted oceanic Moho according to the arch model of *Crosson and Owens* [1987].

Qualitatively, the JDF plate must deform to accommodate the change in strike of the subduction zone from N-S along the Oregon coast to NW-SE off the coast of Vancouver Island. This deformation results in compression within the slab along the strike of the subduction zone. *Chiao and Creager* [1989] have studied the kinematic deformation of the subducted slab and suggest that the arch model reduces the along-strike compressive strain rates and may be the optimal geometric configuration. Their slab model, derived from calculating the in-plane strain-rate field of the CSZ has added further insight into the nature of the arch structure.

The Olympic uplift has been causally linked with the coincident local reduction in dip of the subducted slab beneath the Olympic Peninsula by *Davis and Hyndman* [1989]. Here the gentle dip ($< 10^{o}$) of the slab causes the accretionary prism to grow upward well above sea level to form the Olympic Mountains. The basaltic belts of the Crescent Formation, which comprise the eastern side of the Olympic Peninsula, display a distinct horseshoe outcrop pattern [*Tabor and Cady*, 1978] and this oceanward-concave shape mimics the depth contours of the subducted slab.

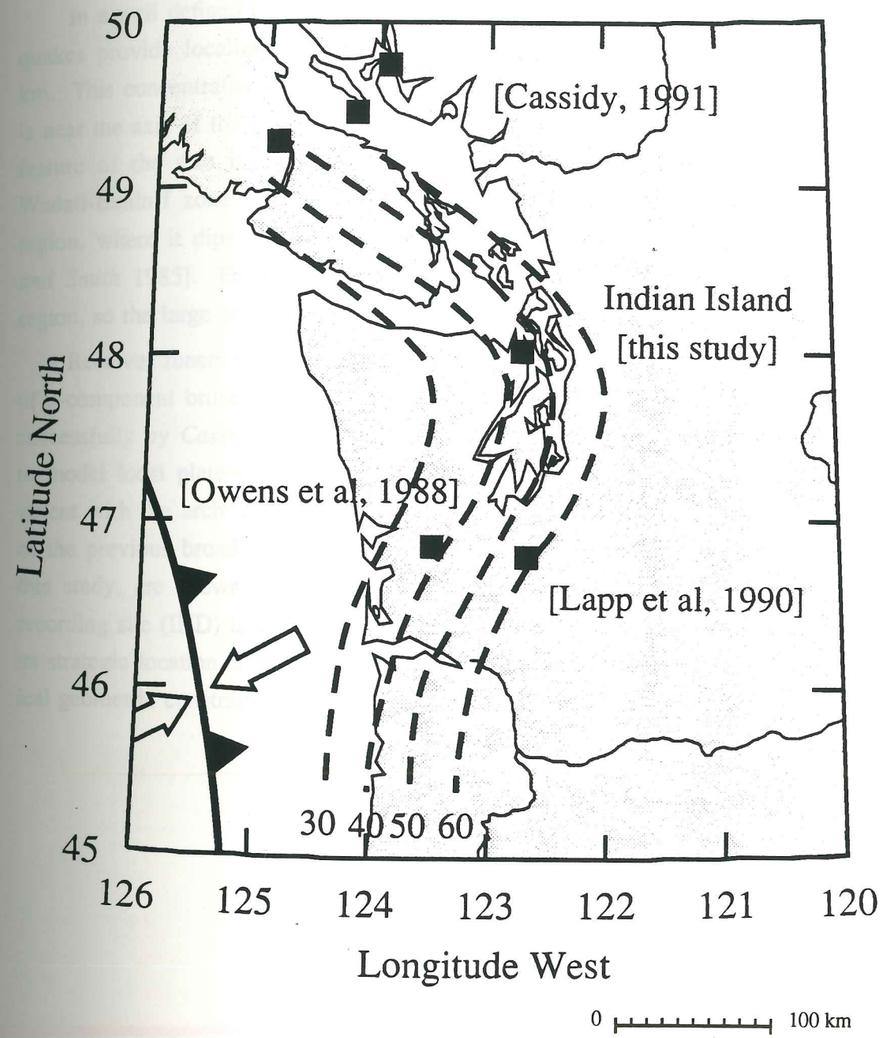

Figure 2.1 Lambert conformal projection of Pacific Northwest map overlain by contour map of shallow subducted slab structure. The contours were inferred with the use of seismicity as well as other data sets including teleseismic receiver function studies [after Crosson and Owens, 1987]. Depth to contours, in kilometers, is shown at the bottom of the figure. Boxes are locations of receiver function study sites.

In a well defined patch beneath central Puget Sound, hypocenters of slab earthquakes provide localized evidence of the arch structure to depths of about 70-80 km. This concentration of slab seismicity (both in number and size of earthquakes) is near the axis of the arch (Figure 2.2). This coincidence suggests that the upwarp feature of the slab is associated with the location of subcrustal earthquakes. A Wadati-Benioff zone to a depth of 100 km exists only beneath the Puget Sound region, where it dips approximately eastward at 10° to 12° [*Crosson* 1983, *Taber and Smith* 1985]. Few earthquakes occur in the subducted slab outside the arch region, so the large scale structure of the slab is only poorly defined by seismicity.

Receiver function studies using teleseismic P-waveforms collected at a number of 3-component broadband stations above the subducting JDF plate have been used successfully by *Cassidy* [1991], *Lapp et al* [1990], and *Crosson and Owens* [1987] to model local plate geometry. Their analyses verify a dipping slab structure consistent with the arch model both to the north and south of Puget Sound. The sites of the previous broadband studies, as well as the Indian Island site investigated in this study, are shown on Figure 2.1 as boxes. The location of the Indian Island recording site (IND) is also shown in the center cross-section on Figure 2.2. Due to its strategic location, analysis of data from Indian Island will provide additional critical geometric constraints of plate structure near the apex of the arch.

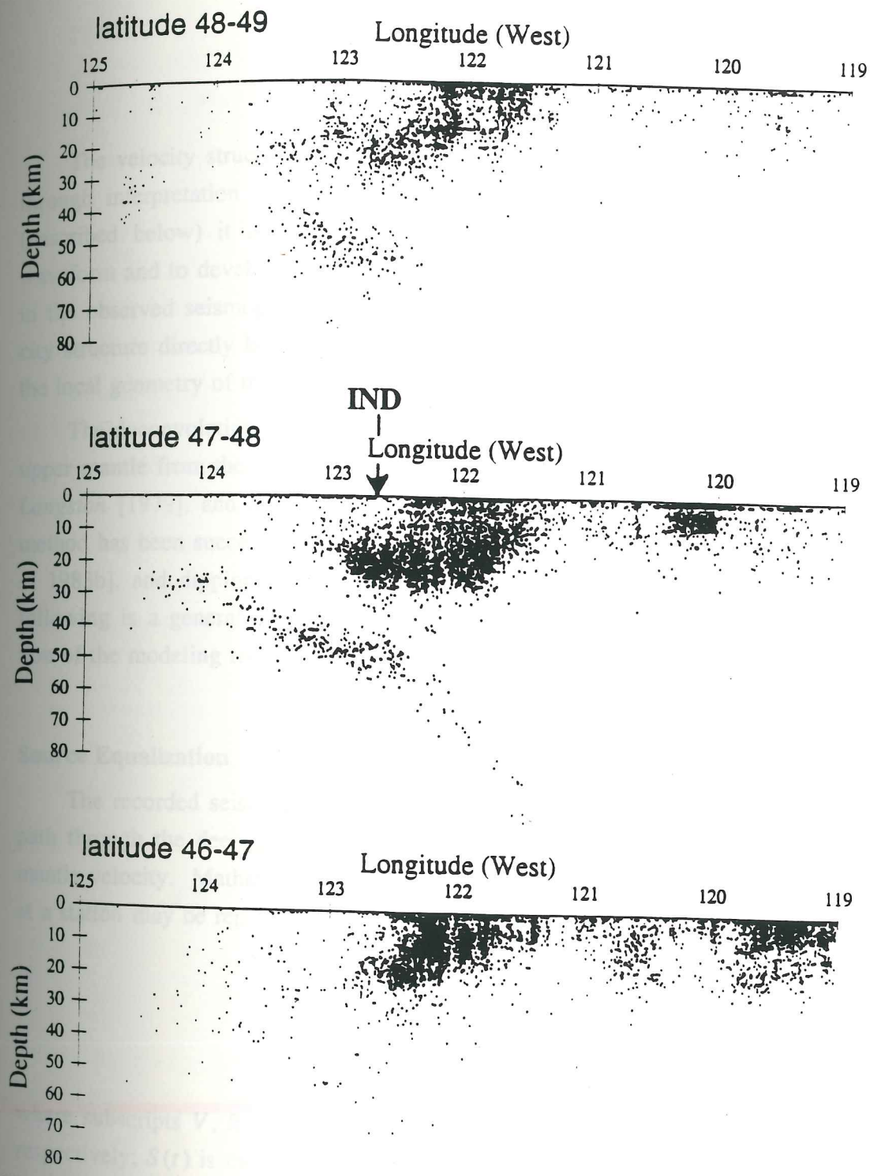

Figure 2.2 Cross-sections of seismicity in Western Washington. Each cross-section represents all earthquakes recorded from 1970 through April 1991 within the indicated degree of latitude. The Indian Island recording site (IND) is shown in the center cross-section. Vertical exaggeration is 2:1.

Chapter 3

Receiver Function Theory

The velocity structure of the crust beneath a recording station can be inferred through interpretation of the teleseismic *P* waveform. Using source-equalization (described below) it is possible to isolate the effects of local structure in the waveform and to develop a simplified velocity model which explains major features in the observed seismograms. Because the effect on the waveform is due to velocity structure directly below the recording station, this method is ideal for imaging the local geometry of the JDF slab.

The deconvolution technique necessary to isolate the response of the crust and upper mantle from the observed teleseismic *P* waveform was initially developed by *Langston* [1979], and has been examined in detail by *Owens et al* [1983a]. This method has been successfully applied to model both horizontal layers [e.g. *Owens et al* 1983b], and dipping structure [e.g. *Owens et al* 1988, *Lapp et al* 1990]. The following is a general outline of the source equalization procedure, and a description of the modeling technique used to identify local structure.

Source Equalization

The recorded seismogram is influenced by: near-source structure, propagation path through the deep mantle, recording instrument response, and crust and upper mantle velocity. Mathematically, the teleseismic *P* wave displacement response, D, at a station may be represented by three components:

$$\begin{aligned} D_V(t) &= S(t) * I(t) * E_V(t) \\ D_R(t) &= S(t) * I(t) * E_R(t) \\ D_T(t) &= S(t) * I(t) * E_T(t) \end{aligned} \tag{3.1}$$

where subscripts V, R, and T represent vertical, radial, and tangential components respectively; $S(t)$ is the seismic source function; $I(t)$ is the impulse response of the recording instrument; $E(t)$ is the impulse response of the earth structure; and asterisks represent the convolution operator.

The receiver functions are defined in the frequency domain by:

$$H_R(\omega) = \frac{D_R(\omega)}{D_V(\omega)} = \frac{E_R(\omega)I(\omega)S(\omega)}{E_V(\omega)I(\omega)S(\omega)} = \frac{E_R(\omega)}{E_V(\omega)}$$

$$H_T(\omega) = \frac{D_T(\omega)}{D_V(\omega)} = \frac{E_T(\omega)I(\omega)S(\omega)}{E_V(\omega)I(\omega)S(\omega)} = \frac{E_T(\omega)}{E_V(\omega)} \tag{3.2}$$

The receiver functions are sensitive to near receiver conversion from *P-to-S* and are thus useful for modeling near receiver structure.

Introducing a minimum allowable level for the amplitude spectrum of the vertical component stabilizes the source equalization deconvolution and avoids dividing by very small numbers due to troughs in the spectrum [*Helmberger and Wiggins* 1971]. The results of the deconvolution are also smoothed by a Gaussian factor to exclude high frequency noise.

Final estimates for the radial and tangential receiver function expressions are, in the frequency domain:

$$H_R(\omega) \approx \frac{D_R(\omega)\bar{D}_V(\omega)}{\phi(\omega)} G(\omega)$$

$$H_T(\omega) \approx \frac{D_T(\omega)\bar{D}_V(\omega)}{\phi(\omega)} G(\omega) \tag{3.3}$$

where

$$\phi(\omega) = \max\left[D_V(\omega)\bar{D}_V(\omega),\ c \cdot \max\left[D_V(\omega)\bar{D}_V(\omega)\right]\right]$$

and

$$G(\omega) = e^{-\omega^2 / 4\alpha^2}$$

In these expressions, c is the minimum allowable spectral amplitude of the vertical component (the water level) expressed as a fraction of the maximum spectral amplitude, α controls the width of the Gaussian pulse, and the bar over D_V indicates its complex conjugate. The water-level, c, can be interpreted as a factor which trades off arrival time resolution with noise level. Our goal is to keep c as small as possible in hopes of better resolving relative arrival time. The width of the Gaussian, α, controls the smoothing of the high frequency noise. For example, for

$\alpha = 5.0$, all frequencies above about 2 Hz are filtered out of the final result. However, this smooths details of the seismograms, possibly reducing our ability to identify distinct phases.

Transformation of (3.3) back into the time domain produces estimates of $H_R(t)$ and $H_T(t)$ respectively. This source equalization technique produces estimated horizontal receiver functions that are impressively similar even for events with quite different source functions. Figure 3.1 illustrates this for two events from the same source area. By isolating the effects of local crustal and upper mantle structure, a simple pulse is produced in particular for *P-to-S* conversions. It is possible to associate arrivals or phases in the waveform with specific velocity-contrast interfaces beneath the station.

Analysis of Subsurface Structure

Receiver functions are most sensitive to *P-to-S* wave conversions at velocity discontinuities directly beneath the recording station. Successful analysis of subsurface structure using receiver functions depends on the ability to model the shear velocity structure with simple geometries such as horizontal or planar dipping layers. The following is a summary of features that are associated with flat and gently dipping structures which may be observed in original seismograms and deconvolved receiver functions.

For vertically heterogeneous structure, *P* waves impinging upon an interface with constant ray parameter produce waveforms which are independent of azimuth. Figure 3.2 shows a sample flat-layer model, and the corresponding vertical, radial, and tangential seismograms generated from this model. The vertical component consists of a direct *P* wave followed by smaller amplitude *P* multiples. The radial component is simply a scaled version of the vertical with the addition of *P-to-S* conversions and *S* wave multiples; there is no off-azimuth or tangential component generated in the flat-layer case.

In the presence of planar dipping structure, the radial seismogram is no longer a simple, scaled version of the vertical, and a tangential component is generated. Figure 3.3 shows a dipping-interface model, and the corresponding vertical, radial, and tangential components of a *P* waveform produced at this interface. The dipping

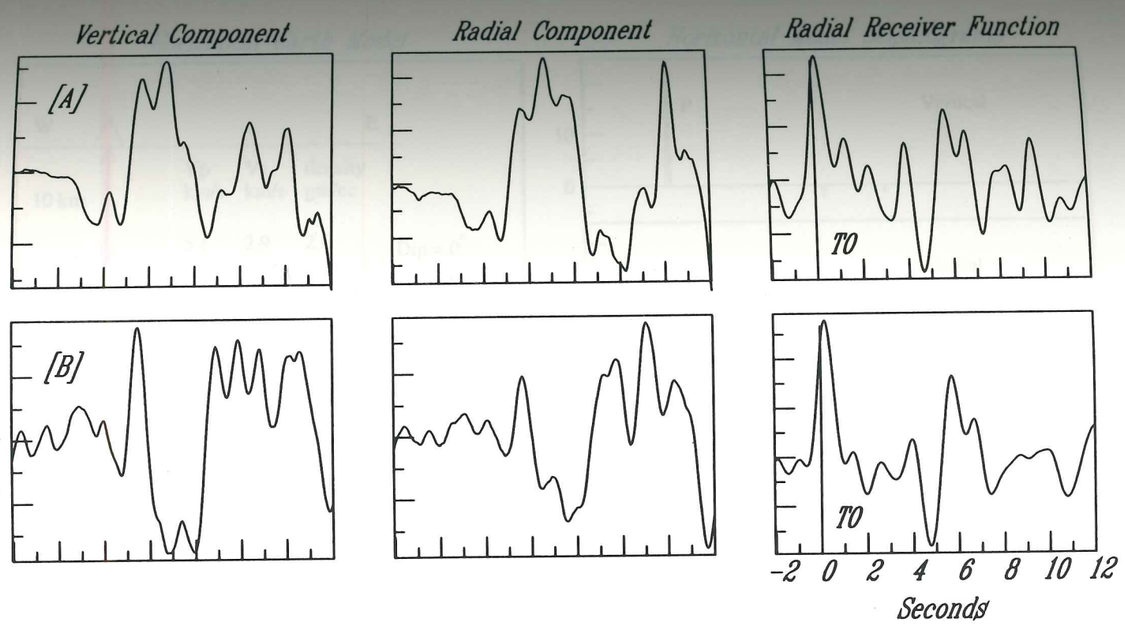

Figure 3.1 Events [A] and [B] from the same source location show quite different vertical and unprocessed radial components. However, several phases on the radial receiver functions are consistently similar.

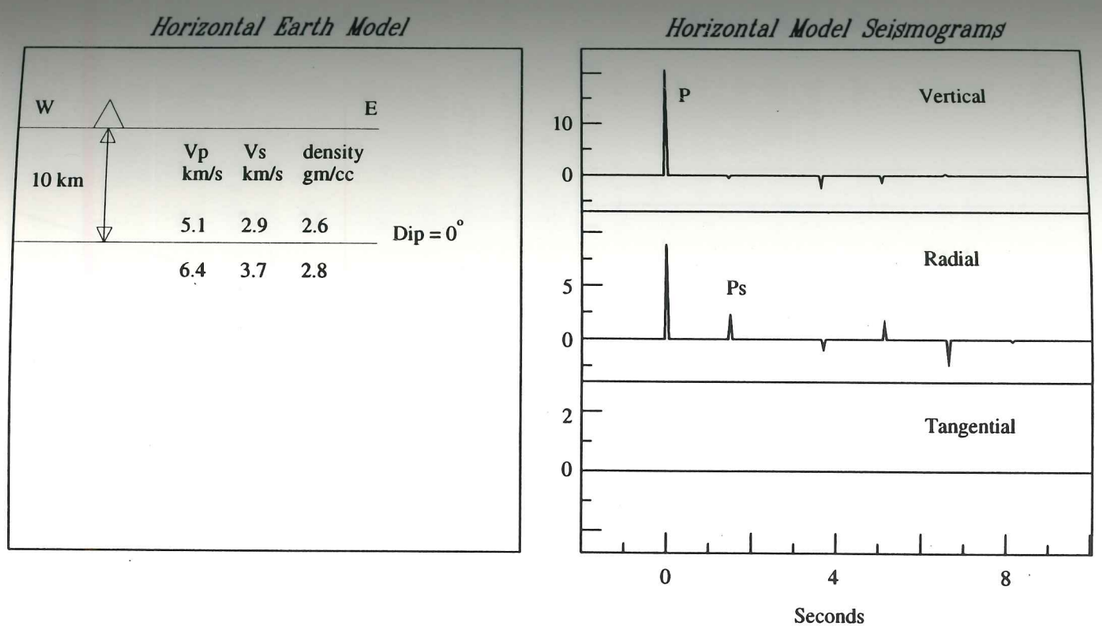

Figure 3.2 Horizontal interface model and synthetic P-waveform components.

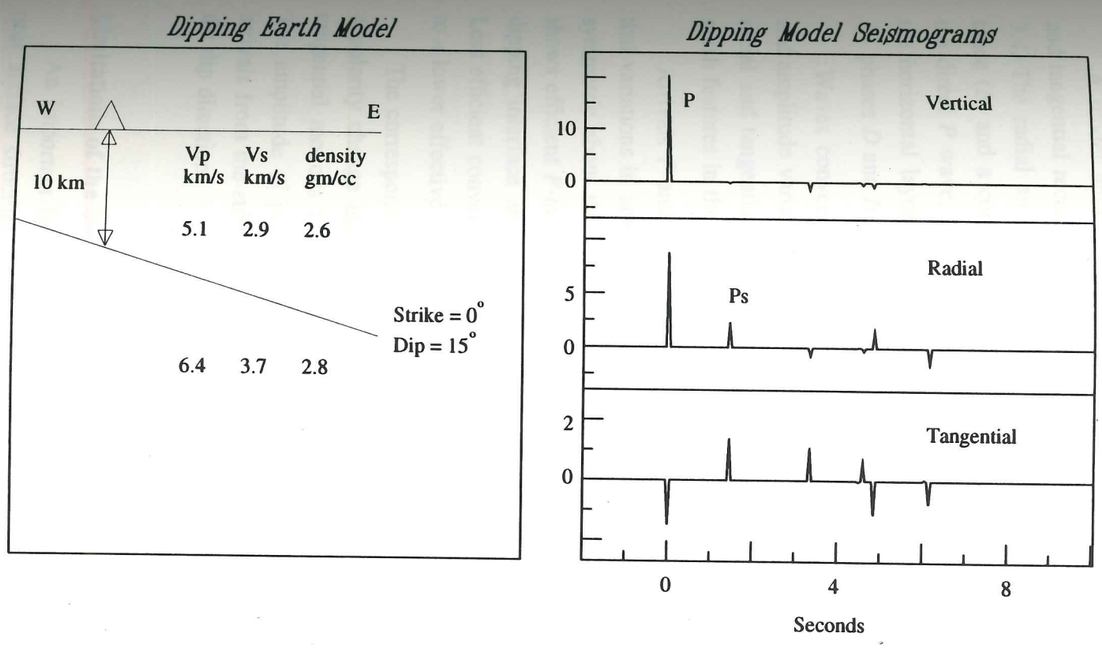

Figure 3.3 Dipping interface model and synthetic P-waveform components.

layer is inclined 15° due east, and the waveform is generated from a source at backazimuth = 360° and distance = 50°.

A model with both a dipping and a horizontal layer, and the synthetic radial and tangential receiver functions generated using this model are illustrated in Figure 3.4. The radial and tangential receiver functions are displayed for a constant distance (Δ) and a complete range of backazimuths. Arrivals labeled *P, D,* and *H* are the direct *P* wave, and the *P-to-S* converted waves from the dipping boundary and the horizontal layer, respectively. Significant differences are apparent between the P_S phases *D* and *H* as a function of backazimuth.

Waves converted at the dipping interface exhibit pulses with distinctive time and amplitude variations that depend on source backazimuth. These variations in the radial and tangential receiver functions can be used in forward modeling to distinguish features in the dipping structure such as strike direction and dip angle.

Arrivals *P* and *D* on the radial receiver functions (Figure 3.4), display azimuthal variations in amplitude. The waveforms are identical for backazimuths that are symmetric about the dip direction. Converted arrival *D* from the up-dip direction shows efficient *P-to-S* conversion due to the high effective angle of incidence at the dipping interface and result in high-amplitude P_S pulses in the receiver function. Less efficient conversion is experienced by arrivals from the down-dip direction due to a lower effective angle of incidence.

The corresponding *P* and *D* arrivals on the tangential receiver functions exhibit a polarity change about the dip direction. As described by [*Langston* 1977], the tangential motions form mirror images across a line parallel to the dip direction. The amplitude of peak *D* is zero for updip and downdip arrivals, and largest for arrivals from the strike direction. This characteristic can be employed to constrain the dip direction.

Limitations of the Technique

An important limitation of the source equalization technique for determining near surface structure is the assumption of laterally homogeneous or moderately dipping structure. The validity of this assumption depends on the lateral extent of the sampled structure; which is roughly equal to the depth of the deepest reflecting

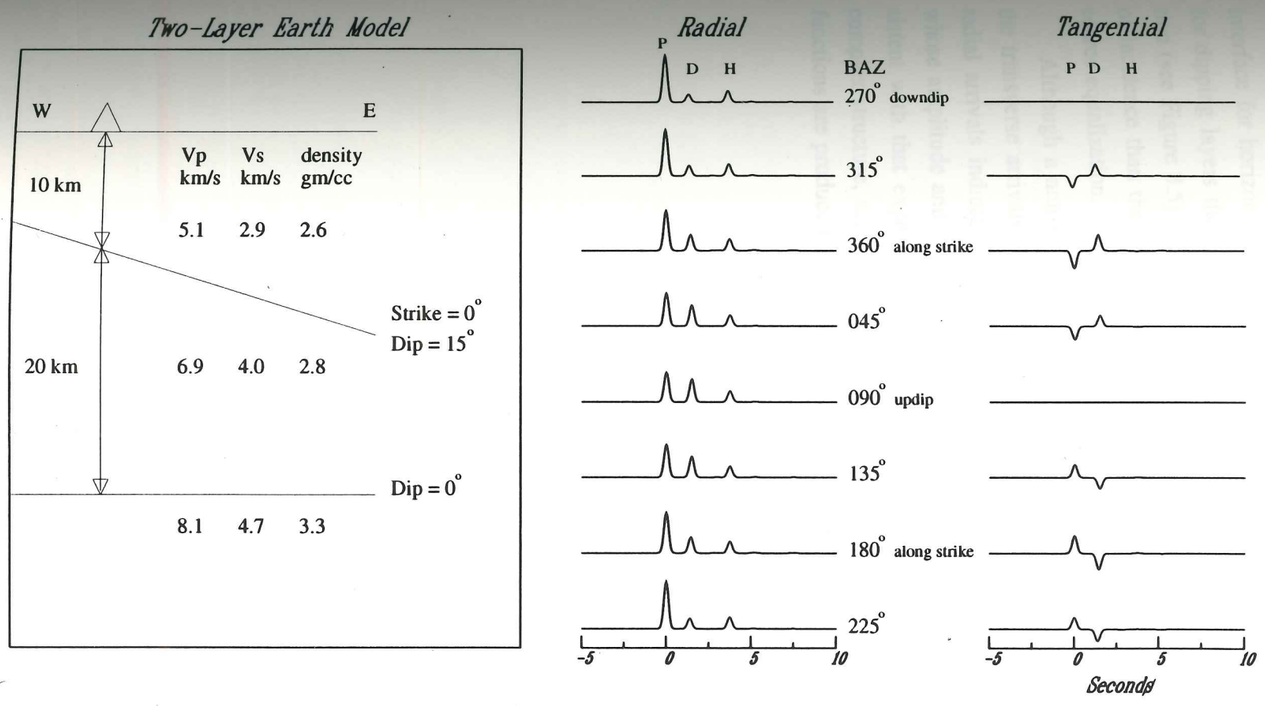

Figure 3.4 Two-layer earth model, and radial and tangential receiver functions. Pulse P is direct P-wave, D is converted wave from the dipping interface, H is from the horizontal layer [after Cassidy, 1991].

interface for horizontal layers [*Ammon et al* 1990]. *Cassidy* [1991] has shown that for dipping layers the lateral extent of sampling shifts to the updip side of the station (see Figure 3.5). *P* wave reverberations arrive at the surface at different angles of incidence than the direct *P* wave and therefore these phases are not removed by source equalization.

Although a non-zero tangential component is an indication of dipping structure the transverse arrivals observed in this dataset are often as large or larger than the radial arrivals indicating complex laterally inhomogeneous structure. Only phases whose amplitude and arrival time variations with backazimuth and distance are consistent with that expected of a P_S phase should be modeled. In the presence of complex structure, such as layers dipping different directions, very complex receiver functions are produced and forward modeling may be impossible or impractical.

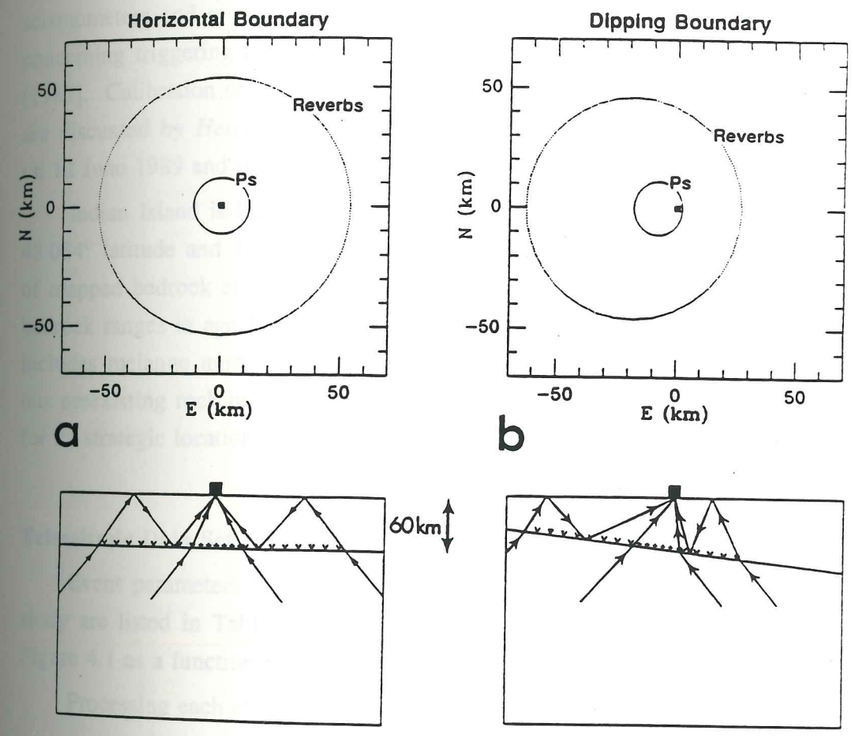

Figure 3.5 Examples of the lateral extent of sampling provided by Ps conversions and reverberations (in both plan view - top and cross-section - bottom) for a horizontal boundary (a), and a dipping boundary (b). In the case of a horizontal boundary a circlular area is sampled; for a dipping boundary the area sampled is offset to the updip side of the station [after *Cassidy,* 1991].

Chapter 4

Data Collection and Processing

The temporary seismic station deployed at the Indian Island site (IND) is equipped with intermediate period (5 second) Kinemetrics SH-1 and SV-1 velocity seismometers and records three components of digital broadband data. For details concerning triggering parameters, and recording and playback procedures see *Lapp* [1987]. Calibration of the seismometers and installation of the recording equipment are discussed by *Hendrickson* [1986]. The seismometers were installed at this site on 12 June 1989 and data was collected for analysis through 7 May 1991.

Indian Island is located north west of Seattle within the Puget Sound basin at 48.034° latitude and 122.710° longitude. The station sits atop stable, gentle slopes of mapped bedrock at the southern end of the island. In Puget Sound, pre-Tertiary bedrock ranges in age from Devonian (360-410 Ma) to Cretaceous (63-138 Ma) and includes melange units, which formed by tectonic deformation and mixing of various preexisting rock units [*Pessel et al* 1989]. The site at Indian Island was chosen for its strategic location near the apex of the proposed arch in the subducted slab.

Teleseismic Data Set

Event parameters for the forty-five teleseismic events collected for use in this study are listed in Table 4.1. The global distribution of these events is shown in Figure 4.1 as a function of azimuth and angular distance from IND.

Processing each of the recorded teleseisms includes:

[1] locating the event in the Preliminary Determination of Epicenters (PDE) listing,

[2] choosing events for which $30^\circ \leq \Delta \leq 100^\circ$,

[3] rotating the horizontal components into radial and tangential orientations,

[4] removing the D.C. offset from the data,

[5] applying a three-second cosine taper to the ends of each trace,

Table 4.1: Event parameters for the earthquakes used in this study. The back azimuth (BAZ) and angular distance (Δ) to each event are caculcated with respect to the Indian Island station (IND).

Events Used in Present Study								
Date	Time	Location		Depth	Magnitude	Δ	BAZ	Stack
yy/mm/dd	(UTC)	Latitude	Longitude	(km)	m_b	(w.r.t. IND)		Group
89/06/25	20:37	1.149N	79.649W	19	5.8	60°	128°	C2
89/08/29	04:16	18.073N	105.627W	34	5.7	33°	149°	D1
89/10/07	16:42	51.116N	179.172W	33	5.6	36°	297°	G1
89/10/07	17:42	51.120N	179.211W	33	5.6	36°	297°	G1
89/10/27	21:04	10.998S	162.382E	29	6.1	88°	251°	F3
89/10/29	05:25	39.546N	143.333E	28	6.0	64°	301°	G4
89/10/29	19:05	36.785N	2.449E	10	5.8	82°	41°	A2
89/11/01	06:40	21.252S	68.099W	143	5.8	85°	130°	C3
89/11/29	01:00	15.781S	73.254W	74	6.1	78°	131°	C3
89/12/03	14:16	7.704S	74.679W	158	5.9	70°	128°	C2
89/12/15	18:43	8.393N	126.778E	33	7.4	97°	291°	G5
90/01/04	05:32	15.046S	172.904W	83	6.4	77°	230°	F1
90/02/19	06:48	15.411S	166.297E	36	6.3	89°	246°	F3
90/02/25	22:51	18.109S	69.299W	141	5.6	81°	129°	C3
90/02/26	19:06	26.732S	114.844W	10	5.7	75°	173°	D2
90/02/27	09:28	17.129S	64.219W	611	5.5	83°	125°	C3
90/03/03	12:16	22.041S	175.156E	33	6.4	89°	235°	F2
90/03/05	16:38	18.134S	167.949E	33	5.6	90°	243°	F3
90/03/25	13:22	9.889N	84.885W	19	6.3	50°	127°	C1
90/03/25	14:17	37.016N	72.959E	32	6.0	94°	348°	H1
90/04/03	22:57	11.397N	86.388W	53	5.9	48°	128°	C1
90/04/05	21:12	15.226N	147.529E	32	6.5	79°	280°	G2
90/04/06	14:57	15.208N	147.560E	33	5.8	79°	280°	G2
90/04/09	09:31	25.659S	176.100W	56	5.8	88°	226°	F2
90/04/11	20:51	35.453N	135.484E	369	5.7	71°	303°	G3
90/05/05	07:21	40.746N	15.850E	26	5.3	84°	30°	A2

Table 4.1: (continued)

Events Used in Present Study								
Date yy/mm/dd	Time (UTC)	Location Latitude	Longitude	Depth (km)	Magnitude m_b	Δ (w.r.t. IND)	BAZ	Stack Group
90/05/08	00:01	6.951N	82.635W	6	6.3	53°	127°	C1
90/05/11	13:10	41.780N	130.881E	580	5.7	69°	310°	G4
90/05/11	23:43	17.333N	100.677W	44	5.3	36°	142°	D1
90/05/12	04:50	49.040N	141.881E	611	6.4	59°	310°	G4
90/05/15	14:25	35.986N	70.443E	117	6.0	95°	349°	H1
90/05/17	23:28	26.614N	127.814E	39	6.1	82°	302°	G3
90/07/10	03:18	10.291S	161.138E	69	5.8	88°	253°	F3
90/10/10	01:00	19.340S	66.551W	271	5.8	84°	128°	C3
90/10/17	14:30	10.970S	70.776W	599	6.7	75°	127°	C3
90/11/06	20:14	53.468N	169.929E	32	6.4	41°	304°	G1
90/12/13	03:01	24.032N	121.669E	14	5.9	88°	304°	G6
91/03/08	11:36	60.828N	167.118E	33	6.3	41°	315°	G1
91/04/14	08:08	27.125N	127.400E	105	6.2	82°	302°	G3
91/04/18	09:41	22.845S	179.442W	474	5.7	87°	230°	F2
91/04/19	11:25	14.924S	175.150W	33	5.6	78°	231°	F1
91/04/22	21:56	9.676N	83.082W	10	6.6	51°	126°	C1
91/04/23	06:34	14.039N	91.667W	65	5.4	43°	132°	C1
91/04/29	09:12	42.489N	43.647E	10	6.2	89°	10°	A1
91/05/07	13:09	39.333N	144.722E	33	6.3	63°	300°	G4

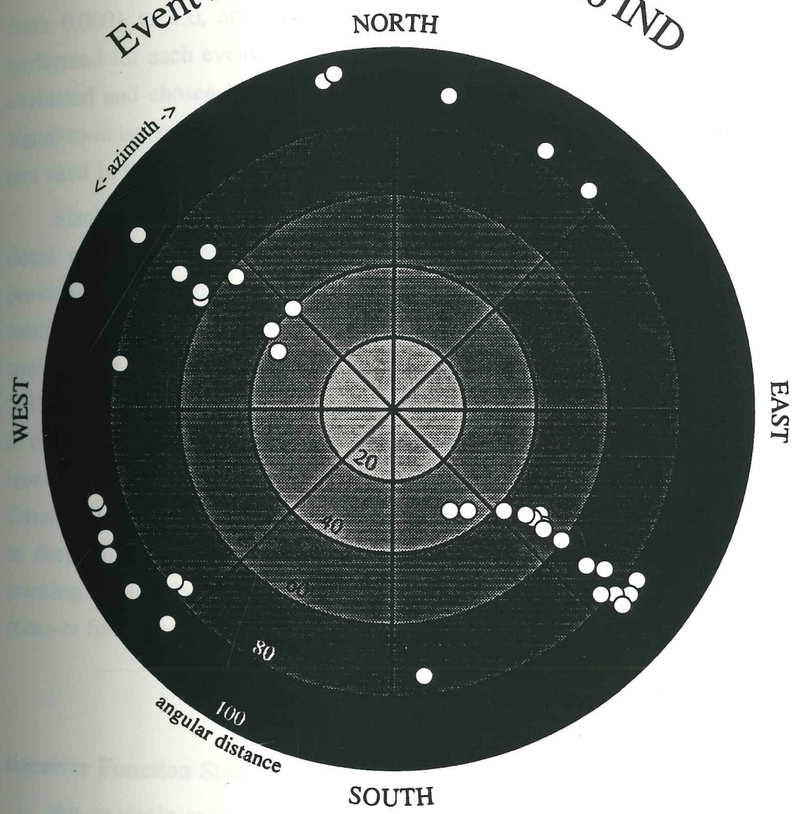

Figure 4.1 Event locations with respect to IND for all events used in the analysis, recorded between 16 June 1989 and 7 May 1991.

[6] performing source equalization, varying the water-level and Gaussian parameters,

[7] stacking the deconvolved components to improve signal-to-noise ratio.

In processing this dataset, the value of the water-level parameter was varied from 0.0001 to 1.0, and the Gaussian parameter used was 5.0. Deconvolution is performed for each event over these parameter ranges and the receiver functions are evaluated and chosen based on the observation of stable, consistent phases and low signal-to-noise ratio. The effects of varying the water-level and Gaussian parameters used in the deconvolution are discussed in detail by *Owens et al* [1983a].

Stacking the deconvolved components improves the signal-to-noise ratio, produces a single estimate of the receiver function from a particular source area, and provides an error bound for evaluating the fit of the synthetic signals generated from forward modeling. The criteria used for stacking the deconvolved data in this analysis are somewhat stricter than the guidelines recommended by *Owens et al* [1983a] of: $\pm 20^{o}$ in back azimuth, $\pm 15^{o}$ in distance for distance $> 70^{o}$, and $\pm 10^{o}$ in distance for distance $< 70^{o}$. Their criteria were developed for predominantly horizontally layered media. For this analysis we use stacking criteria suggested by *Cassidy* [1991], who demonstrated that to avoid attenuating *P-to-S* phases generated at deep dipping boundaries, both the back azimuth and distance ranges used in stacking should be $\leq 10^{o}$. The resulting thirteen stacked and four single-event receiver functions represent an estimate of the local structure response.

Receiver Function Stack Suites

An example radial and tangential component stack suite is shown in Figure 4.2. All other stack suites used in this study are shown in Appendix A. Each suite consists of the deconvolved signals for each event, plotted above the resulting stacked signal. Each event is identified by back azimuth (*BAZ*) and angular distance (Δ). Stacked and single receiver functions are shown in Figures 4.3 through 4.5. Figure 4.3 displays stacks at a range of distances for backazimuth $\approx 128^{o}$, and for backazimuth $\approx 300^{o}$. Figures 4.4 and 4.5 show radial and tangential stacks and

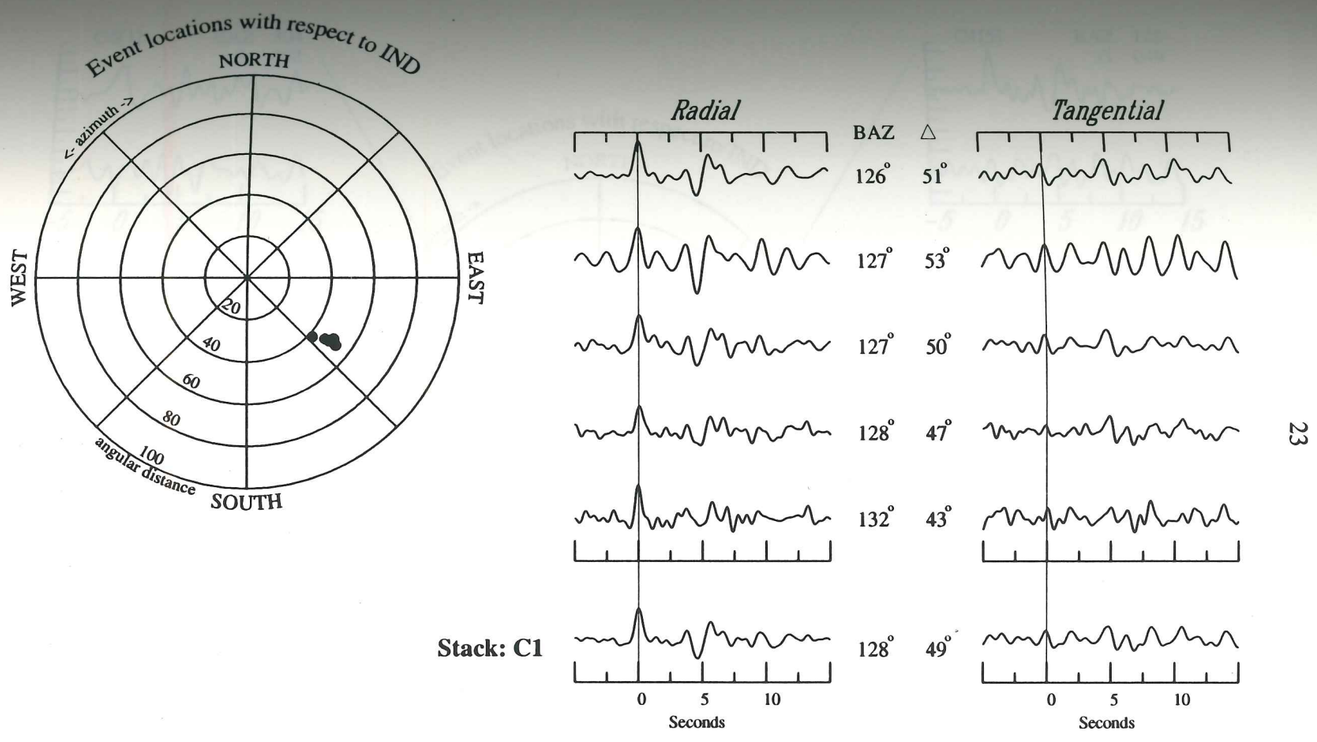

Figure 4.2 Event locations with respect to IND, and radial and tangential receiver functions for events in stacking suite C1. Stack backazimuth and distance are averaged from events in the stack.

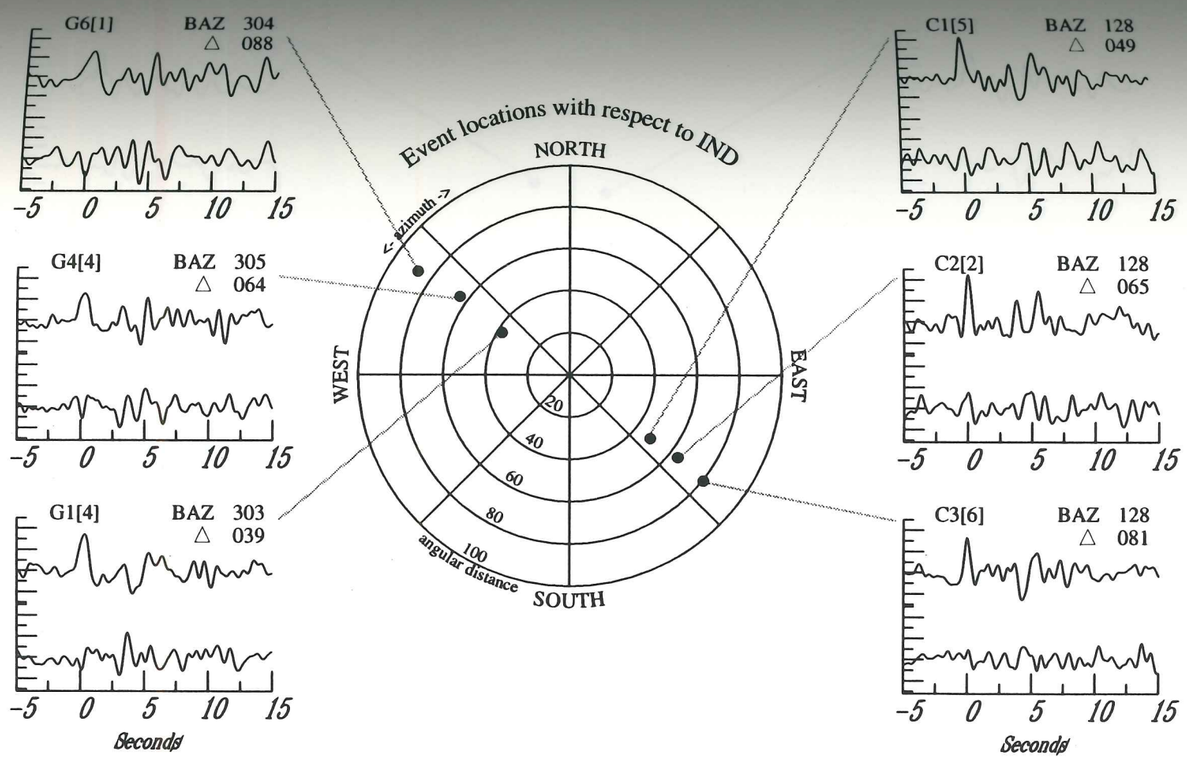

Figure 4.3 Receiver function stacks and single events at a range of backazimuths and distances. Each set shows radial (top) and tangential (bottom) components and is identified by backazimuth, distance, and number in stack.

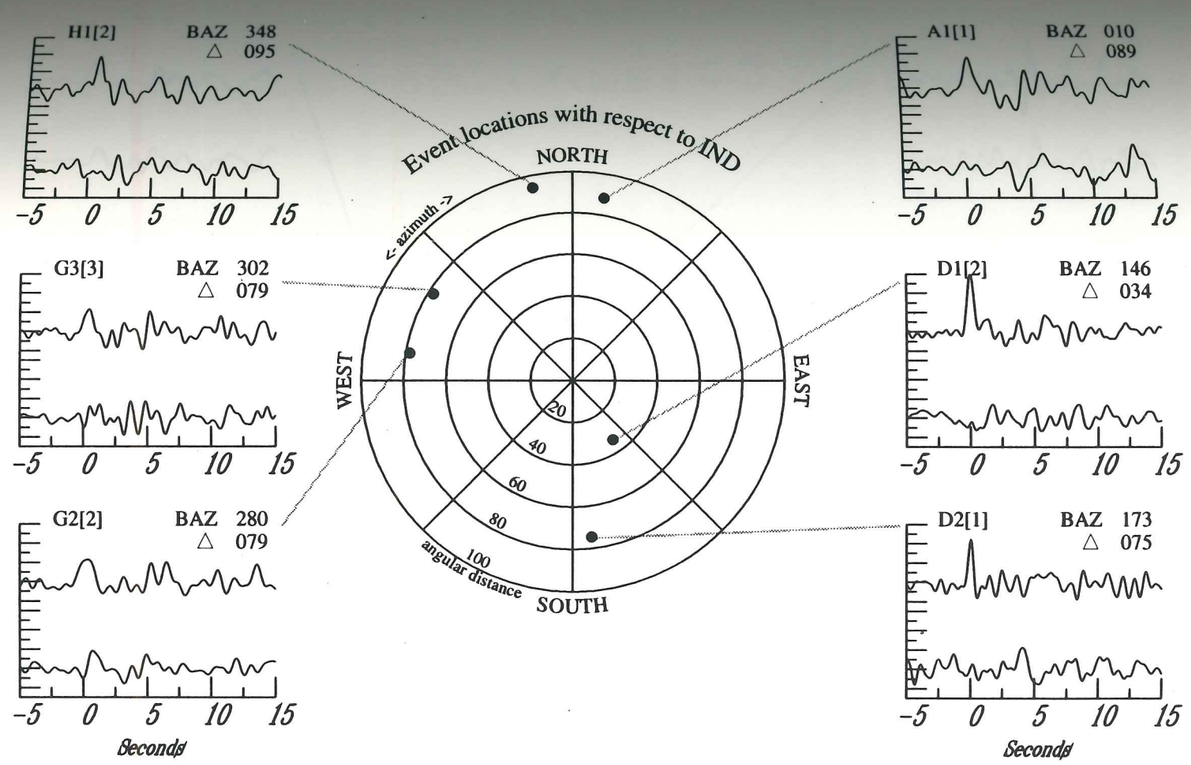

Figure 4.4 Receiver function stacks and single events at a range of backazimuths and distances. Each set shows radial (top) and tangential (bottom) components and is identified by backazimuth, distance, and number in stack.

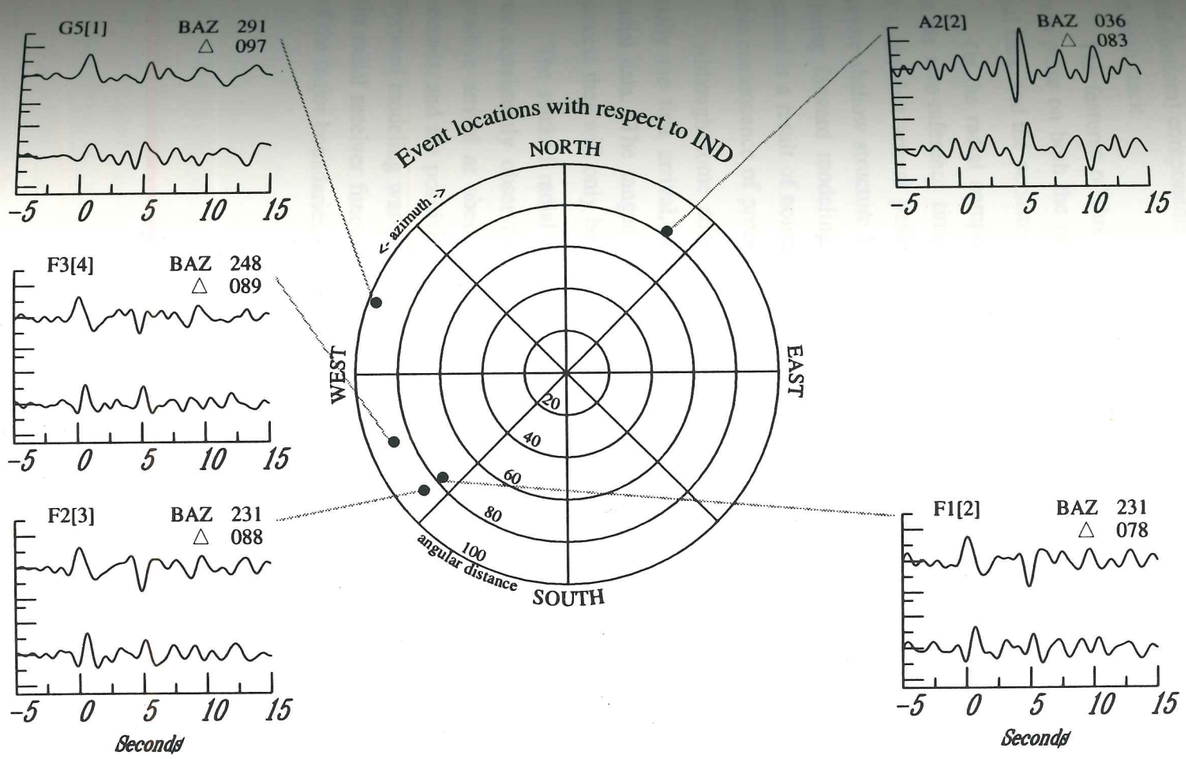

Figure 4.5 Receiver function stacks and single events at a range of backazimuths and distances. Each set shows radial (top) and tangential (bottom) components and is identified by backazimuth, distance, and number in stack.

single events at a range of backazimuths. Each set shows radial (top) and tangential (bottom) components and is identified by backazimuth, distance, and the number in each stack.

The features of this data that will be examined are: the character of the time-zero pulse on both the radial and tangential components, the quality of the tangential data, and the persistence of large-amplitude arrivals on the radial components.

On the radial component, the direct *P* wave should appear as a peak centered at the zero-reference time. However, for several stacks (e.g. *A1, G2, H1* on Figure 4.4) the first arrival peaks are noticeably delayed. This time delay is evidence of severe shallow structure beneath the recording station and will be analyzed in detail during forward modeling. The development of side lobes on the impulsive first arrival is a result of noise introduced by the water level parameter; it is an unavoidable consequence of processing band-limited data [*Owens et al* 1983a].

Although some consistent arrivals are observed in the tangential data, especially the first arrival, they contain a much lower signal-to-noise ratio than the radial data. The tangential component data will not be included in the modeling process they will only be used in qualitative analysis of deeper interfaces.

The stacked radial receiver functions show that only a few coherent arrivals are consistently observed after the prominent direct phase. Most notable are the positive arrival at about four seconds, the negative pulse between four and five seconds, and the positive arrival between five and six seconds after the initial pulse. Forward modeling was performed to reproduce these prominent features observed in the radial receiver functions and will be analyzed to infer the depth and orientation of the major boundaries beneath IND.

Chapter 5

Forward Modeling

Forward modeling of receiver functions requires approximating the true velocity structure with a simplified geometric model, and then determining the right combination of layer thickness, strike direction, dip angle, and velocity that consistently match the amplitude and timing features for events from a wide range of backazimuths. As in other receiver function studies in the Puget Sound [*Lapp et al* 1990 and *Owens et al* 1988], the starting velocity structure for the forward modeling performed in this study was based on a model which incorporates the results of several regional seismic studies. The crustal model of *Taber and Smith* [1985] was combined with average values of the upper mantle [*Zervas and Crosson* 1986] and subducting slab [*Taber and Lewis* 1986] velocities. The average crustal *P* wave velocity is 5.9 km/sec with a 1.0 km/sec contrast at the Moho and the upper mantle *P* wave velocity is 8.0 km/sec. A V_p / V_s ratio of 1.73 has been constrained by analysis of local travel time data.

Synthetic seismograms were generated using the 3-D ray-tracing scheme for planar dipping boundaries described by *Langston* [1977]. Parameters which are specified for each layer include: *P* wave and *S* wave velocities, density, strike and dip angles, and thickness. Independent evidence constrains the average velocities in the region so estimates of layer thickness, dip angle, and dip direction will be obtained by generating synthetic receiver functions and then trial-and-error matching the width, shape, and amplitude of the derived signals with the real receiver functions.

Synthetic radial and tangential receiver functions are produced by processing the synthetic seismograms in the same manner and using the same deconvolution parameter values as the real data. The deconvolution algorithm provided by T. Owens (based on *Langston* [1979]) and subsequently enhanced by C. Ammon preserves the absolute amplitude ratio of P_r / P_z. *Cassidy* [1991] demonstrated that the use of the absolute amplitude is robust, especially in the presence of shallow ($\leq$ 3 km deep) dipping structure, and that using the information preserved in the absolute amplitude helps develop a more accurate earth model. Absolute

amplitudes are used in this study in the comparison of real and synthetic receiver function waveforms.

When comparing synthetic and real receiver functions from a dipping layer environment, emphasis is placed on matching the relative time and amplitudes of consistent, stable arrivals in the radial receiver functions. Arrivals with similar amplitudes and simultaneous arrivals in time for a range of backazimuths are interpreted as conversions though a flat layer, while dipping layers may be recognized by time and amplitude azimuthal variations in both the radial and tangential receiver functions. Reverberations in the signal make this matching process challenging.

Three features of the sub-crustal velocity structure will be investigated by matching synthetically derived receiver functions to the deconvolved real data. On the stacked radial receiver functions these areas can be identified as: the structure of the shallow crust, arrivals from zero to about three seconds; the continental Moho, near three an one-half seconds; and the subducted JDF slab, the negative-to-positive pair of pulses occurring between four and six seconds after the zero reference time.

Shallow Crust Model

Phases arriving within the first second of a receiver function are generated by near surface structure. Evidence for non-horizontal shallow structure may be observed in both the radial and tangential receiver functions. Complex shallow structure is typically observed in the radial deconvolved receiver function by an azimuth-dependent delay of the direct arrival at time zero [*Owens and Crosson* 1988]. This delay is the result of an extremely efficient *P-to-S* conversion through a near surface dipping structure so that the first arriving energy in the waveform is dominated by P_S, not the direct P wave.

Figure 5.1 displays the first four seconds of some typical stacked receiver functions from IND. The radial component in the event from the southeast ($BAZ = 128^{\circ}$, $\Delta = 81^{\circ}$) shows a sharp direct P arrival centered at the zero reference time. However, in signals from the west ($BAZ = 248^{\circ}$, $\Delta = 89^{\circ}$ and $BAZ = 291^{\circ}$, $\Delta = 97^{\circ}$) the shape of the initial pulse has broadened and the main arrival occurs from 0.25 up to 0.4 seconds after time-zero. Receiver functions from

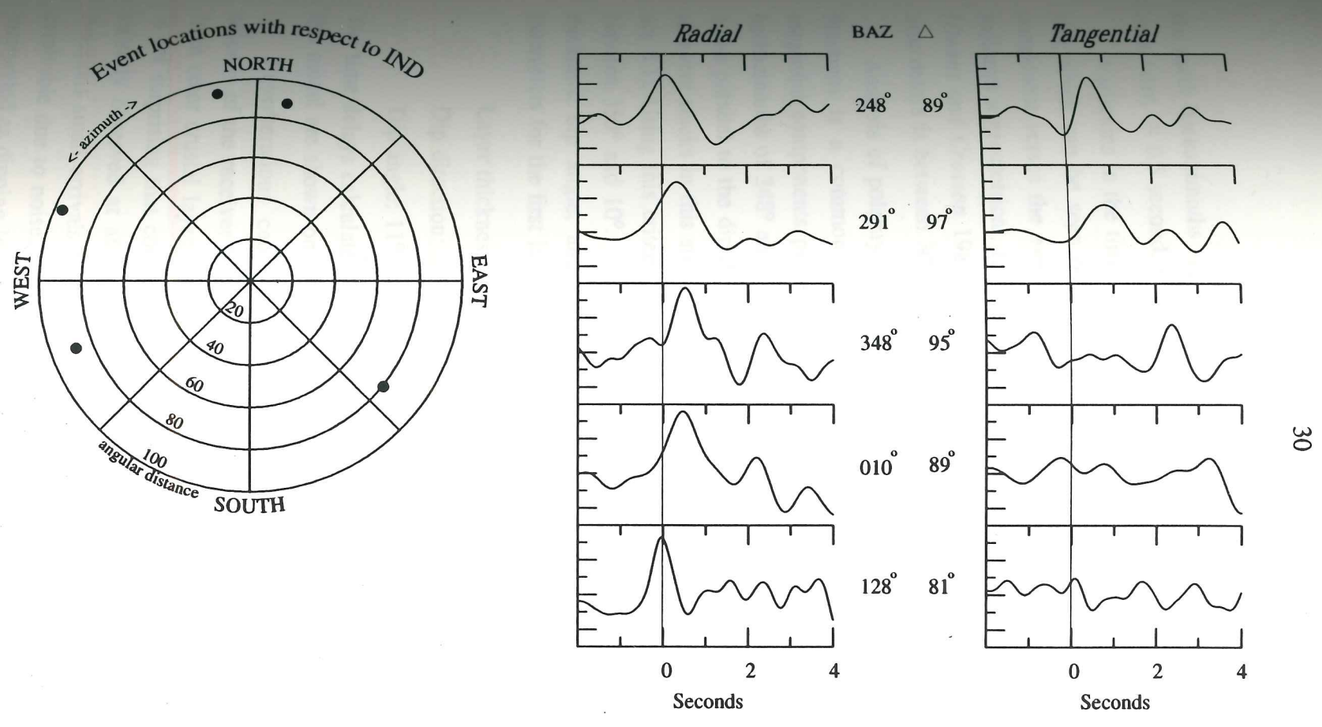

Figure 5.1 Radial and tangential receiver functions for five events recorded at IND. Zero time is direct P-wave arrival time. Note largest radial time delay, and polarity change on tangential between 348 and 010 degrees.

the north backazimuths (BAZ = 348°, Δ = 95° and BAZ = 10°, Δ = 89°) display an even later, ≃ 0.5 second, first arrival.

Variations in the time delays of the first-arriving energy occur in a distinct pattern which can be seen by plotting the time delay of the first pulse on the radial component versus the event backazimuth (Figure 5.2). This azimuthal dependence indicates a geometrical, rather than instrumental, source of the apparent time delays [*Owens and Crosson* 1988]. The range of possible dip directions inferred from the time delays is between 305° and 36° (dashed, vertical lines on Figure 5.2.).

Analysis of polarity changes observed on the tangential components of receiver functions is a common interpretation method for non-horizontal structure. The tangential components plotted in Figure 5.1 exhibit a polarity reversal between the backazimuths of 348° and 10°. Since transverse motions form mirror images across a line parallel to the dip direction, a plot of the tangential first arrival polarities for all event stacks in this study can be used to further constrain the dip direction (Figure 5.3). Using this criteria, the shallow interface dip direction is ascertained to be between 350° and 10°. The first-arrival time delay is quite sensitive to changes in thickness, dip angle, and dip direction. From forward modeling, the structural parameters for the first layer are estimated to be:

Layer thickness: 2.1 km ± 0.5 km

Dip direction: N 5° W ± 5°

Dip angle: 11° ± 3°

The time delays calculated for the synthetic radial receiver functions generated from this model are shown on Figure 5.2 as a dashed, bell-shaped curve.

Reverberations caused by shallow structure may complicate the first few seconds of the receiver functions and be large enough to obscure arrivals generated from other crustal layers. Due to the presence of shallow structure beneath IND it is not surprising that converted arrivals from other near surface layers are not consistently observed at all backazimuths. However, on many of the radial receiver functions small arrivals before ≃ 2.5 seconds are observed. The amplitudes are not resolvable due to noise, and do not appear to be azimuth-dependent so they are not interpreted as dipping layers. The shallow structure model for the first few layers is

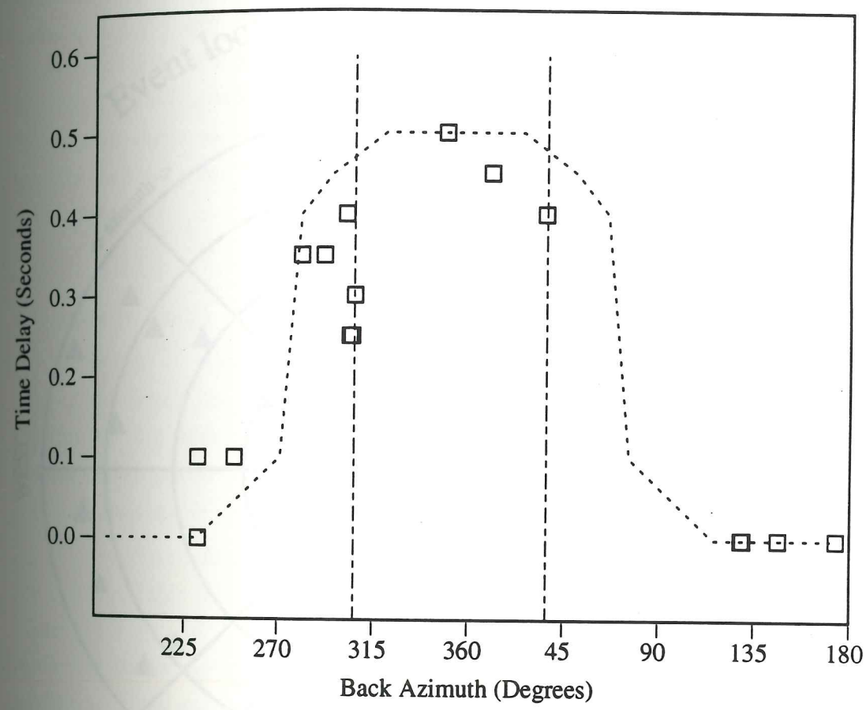

Figure 5.2 Time delay of first pulse on radial component versus event backazimuth for IND site. Vertical lines at 305 and 36 degrees show bounds on dip direction inferred from time delays. Dashed, bell-shaped curve is theoretical delay from the preferred model described in text.

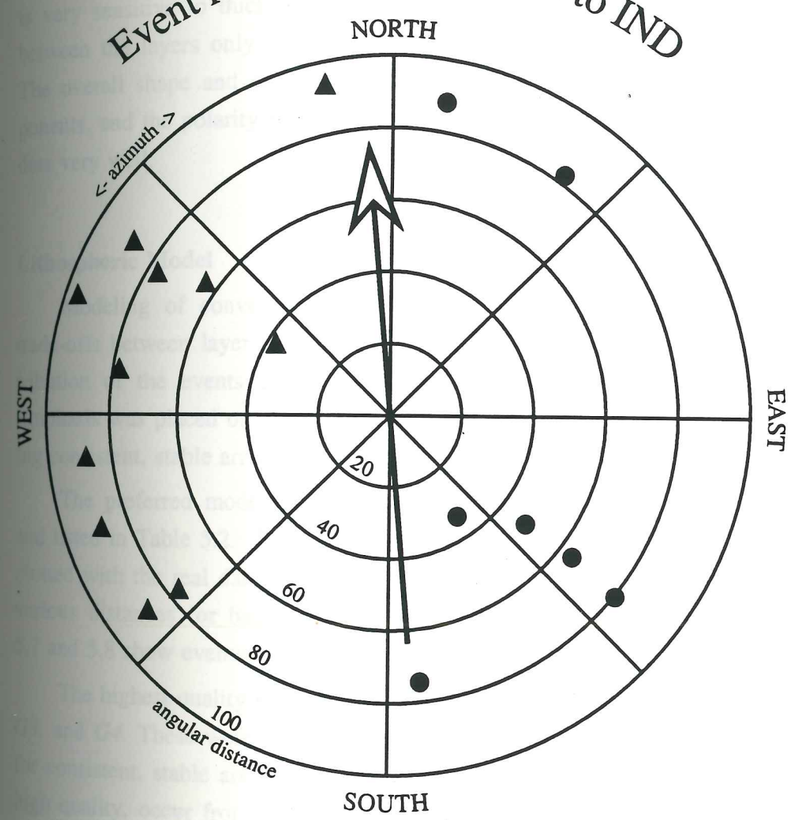

Figure 5.3 Polarities of tangential components versus backazimuth and angular distance. Circles indicate positive polarity, triangles indicate negative polarity. Arrow points in direction of dip in the preferred shallow model.

shown in Table 5.1 and the synthetic receiver functions generated from the shallow-crust model are compared to examples of the observed data in Figure 5.4. The amplitude of the time-delayed peaks is slightly lower than predicted by the synthetic data and many attempts were made to reduce the amplitude. The time delay is very sensitive to thickness and dip angle, and reducing the velocity difference between the layers only succeeded in doing away with the time delay altogether. The overall shape and character of the first-arrival time delay on the radial components, and the polarity reversal on the tangential components match the observed data very well.

Lithospheric Model

Modeling of converted arrivals in the presence of dipping layers involves trade-offs between layer velocity, dip angle, and dip direction. The azimuthal distribution of the events also constrains the range of possible parameters values. Emphasis was placed on modeling the highest quality receiver functions and matching consistent, stable arrivals to obtain the best estimate of local structure.

The preferred model for the lithospheric structure is illustrated in Figure 5.5 and listed in Table 5.2. The radial receiver functions generated from this model are plotted with the real data in Figures 5.6 through 5.8. Figure 5.6 displays events at various distances for backazimuth $\simeq 128^{o}$, and for backazimuth $\simeq 300^{o}$. Figures 5.7 and 5.8 show events for a range of backazimuths and distances.

The highest quality radial receiver functions are those labeled: *C1, C2, C3, G1, G3,* and *G4.* These were chosen due to the relatively high signal-to-noise ratio and for consistent, stable arrivals. Event stacks *H1, A1,* and *A2,* while not of unusually high quality, occur from strategic azimuthal locations and so are very important in modeling. The receiver functions *D1, D2, G2, G5,* and *G6* have good fits to the synthetic model, but the presence of reverberations and noise prevents a great signal match. Receiver function stacks: *F1, F2,* and *F3* have particularly bad fits even though their radial component signal-to-noise ratio is often very high. These anomalous waveforms will be discussed later in this chapter, after all modeled phases are noted.

Table 5.1

Shallow Structure Model						
Layer number	V_P (km/sec)	V_S (km/sec)	Density (g/cc)	Thickness (km)	Strike (degrees)	Dip (degrees)
1	3.00	1.73	2.60	2.1	265.00	11.00
2	5.10	2.95	2.60	2.8	0.00	0.00
3	5.90	3.41	2.70	6.0	0.00	0.00
4	6.30	3.64	2.75	7.0	0.00	0.00
5	6.70	3.87	2.80		0.00	0.00

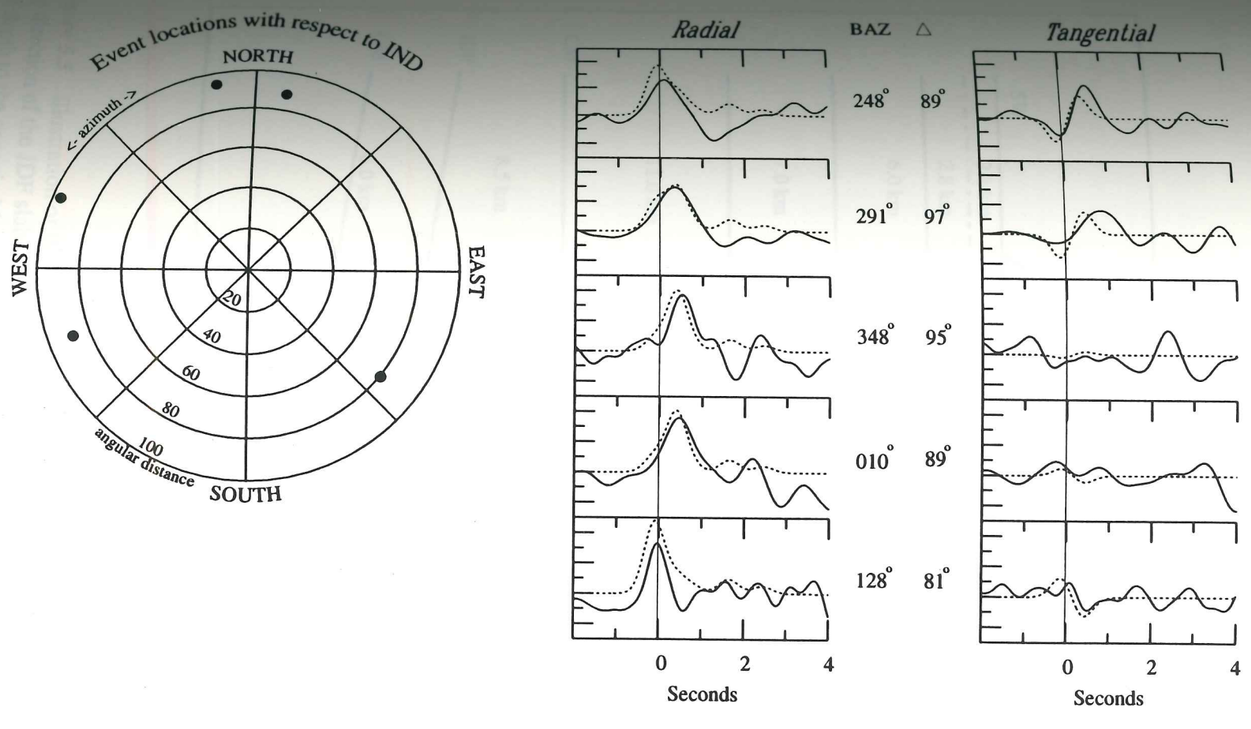

Figure 5.4 Observed (solid) radial and tangential receiver functions for five events recorded at IND. Synthetic (dashed) receiver functions are generated from shallow structure model discussed in text.

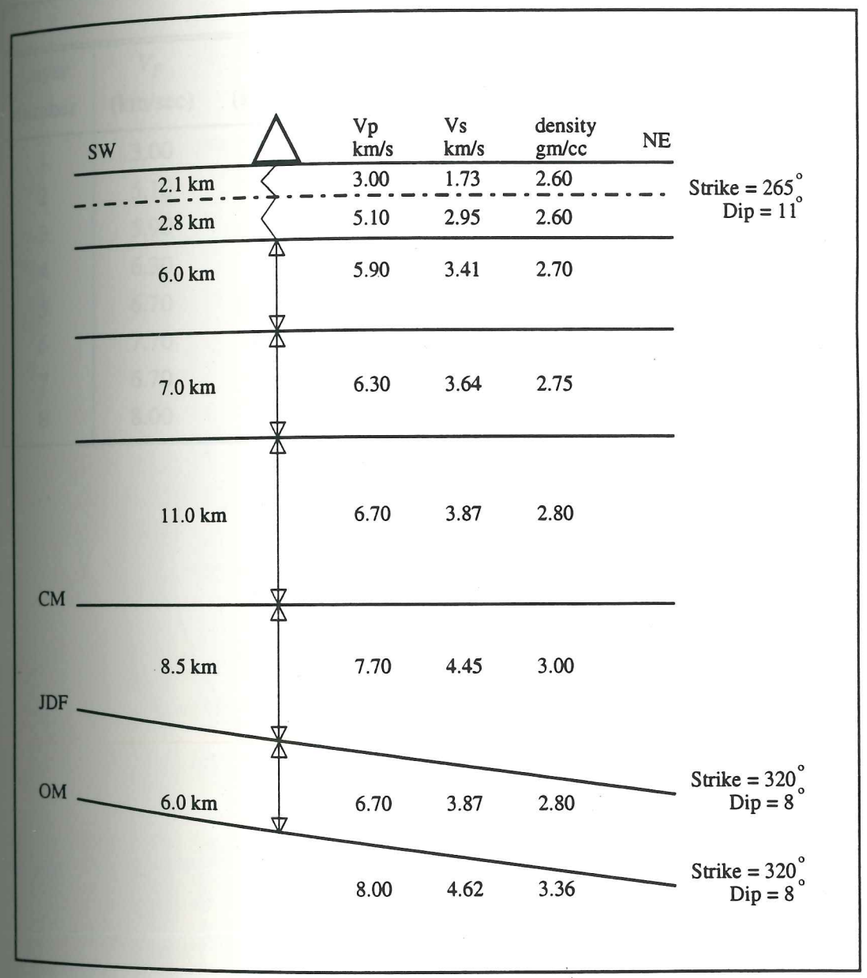

Figure 5.5 Illustration of the preferred lithospheric model, cross-section is along the dip direction of the JDF slab. The depth to the continental Moho (CM) is 28.9 km, and the depth to the oceanic Moho (OM) is 43.4 km.

Table 5.2

Lithospheric Model						
Layer number	V_P (km/sec)	V_S (km/sec)	Density (g/cc)	Thickness (km)	Strike (degrees)	Dip (degrees)
1	3.00	1.73	2.60	2.1	265.00	11.00
2	5.10	2.95	2.60	2.8	0.00	0.00
3	5.90	3.41	2.70	6.0	0.00	0.00
4	6.30	3.64	2.75	7.0	0.00	0.00
5	6.70	3.87	2.80	11.0	0.00	0.00
6	7.70	4.45	3.00	8.5	320.00	8.00
7	6.70	3.87	2.80	6.0	320.00	8.00
8	8.00	4.62	3.36		0.00	0.00

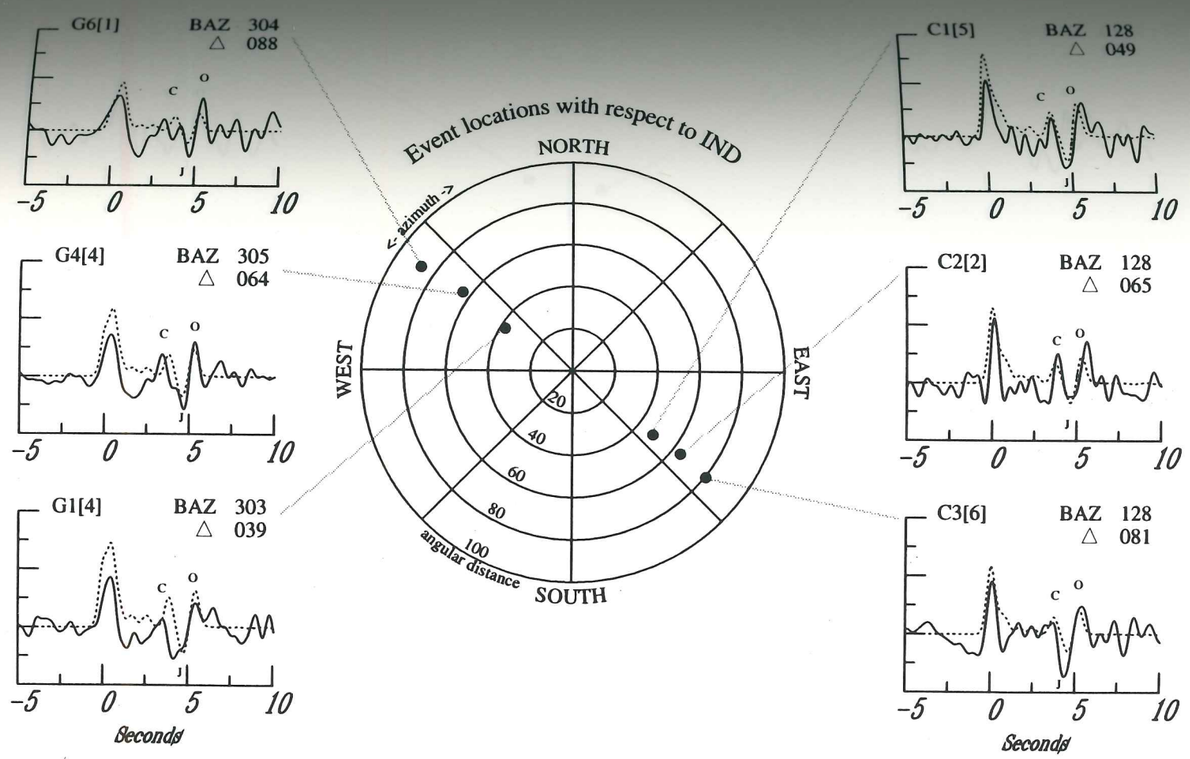

Figure 5.6 Radial observed (solid) and synthetic (dashed) receiver functions at a range of backazimuths and distances for lithospheric model illustrated in Figure 5.5. Labels C, J, and O represent converted phases through the continental Moho, the top of the JDF slab, and the oceanic Moho, respectively.

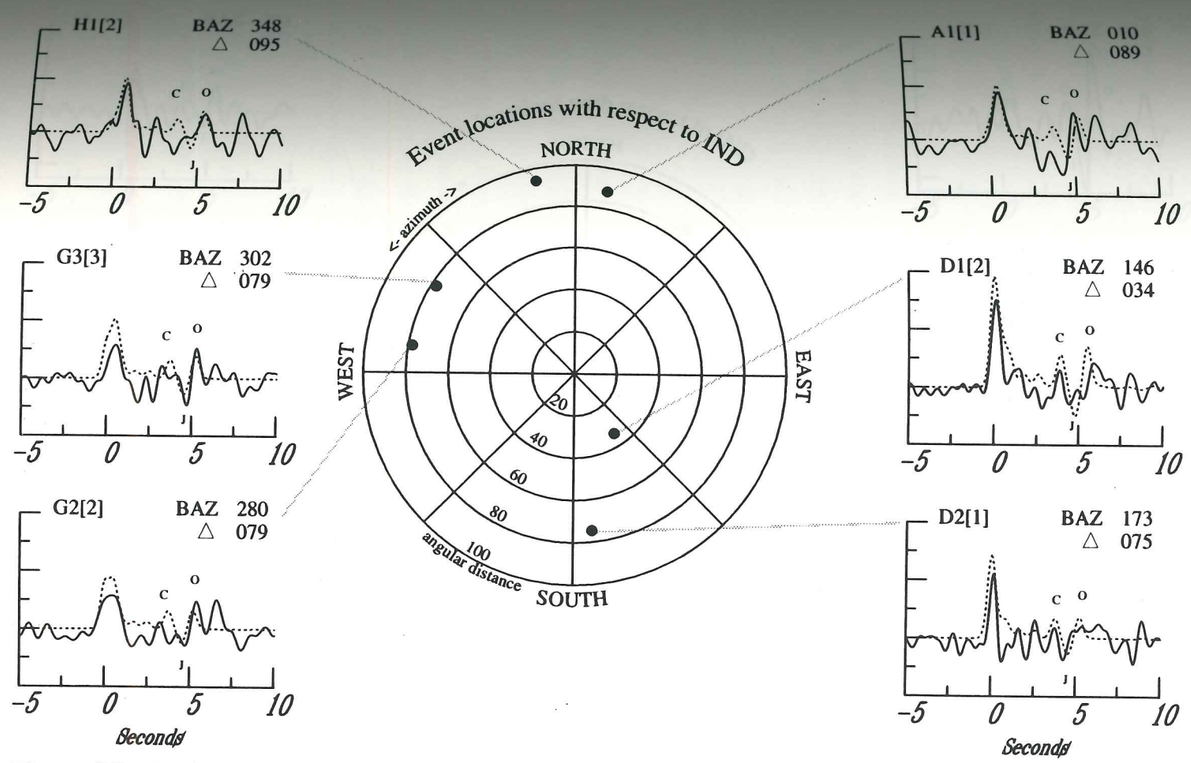

Figure 5.7 Radial observed (solid) and synthetic (dashed) receiver functions at a range of backazimuths and distances for lithospheric model illustrated in Figure 5.5. Labels C, J, and O represent converted phases through the continental Moho, the top of the JDF slab, and the oceanic Moho, respectively.

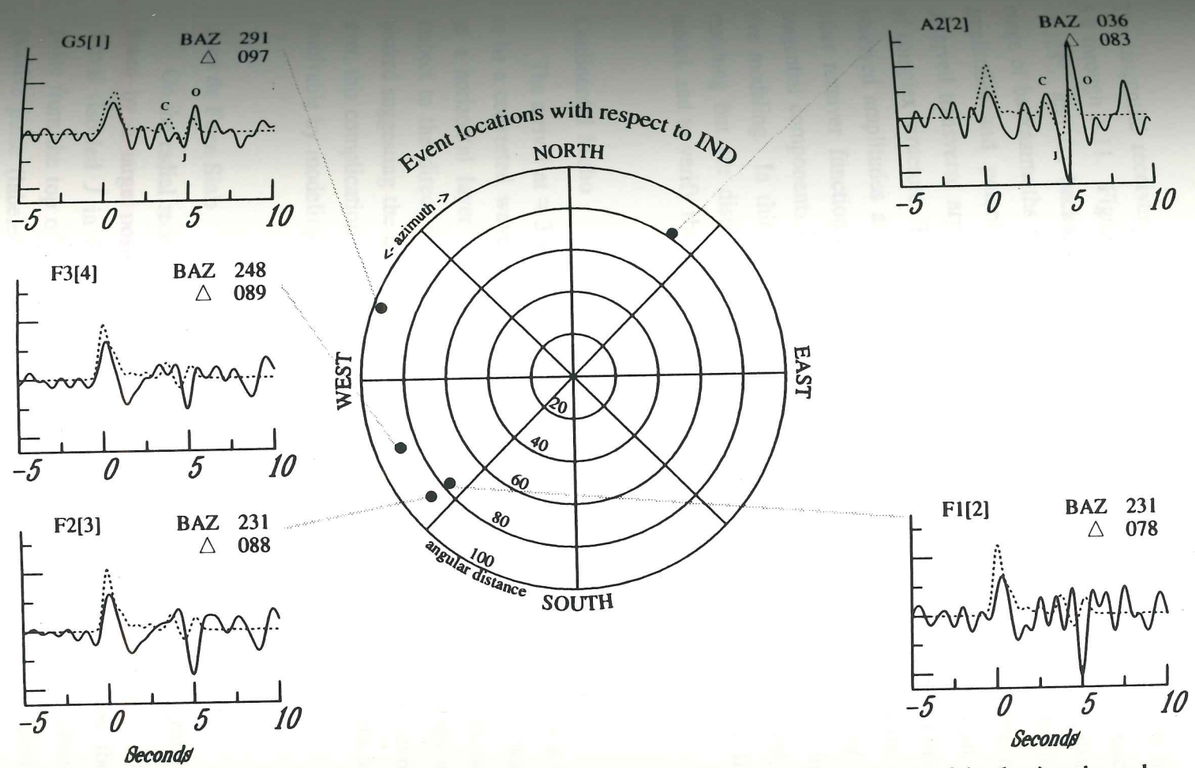

Figure 5.8 Radial observed (solid) and synthetic (dashed) receiver functions at a range of backazimuths and distances for lithospheric model illustrated in Figure 5.5. Labels C, J, and O represent converted phases through the continental Moho, the top of the JDF slab, and the oceanic Moho, respectively.

The tangential receiver functions generated from this model are shown in Figures 5.9 through 5.11. Figure 5.9 displays events at various distances for backazimuth $\simeq 128^{o}$, and for backazimuth $\simeq 300^{o}$. Figures 5.10 and 5.11 show events for a range of backazimuths and distances. As observed above, the synthetic first arrival amplitudes and polarity match the observed data well. There are also large observed transverse arrivals between three and six seconds, which is an indication of complex structure. The tangential waveforms are in general very noisy and the observed amplitudes are much larger than predicted by the lithospheric model. In other receiver function studies [e.g. *Lapp et al* 1990 and *Owens et al* 1988] the tangential components have been found interesting but not very useful in quantitative modeling. In this study, the tangential components were not used for signal matching but are displayed for qualitative comparison with the final lithospheric model, and to verify the presence of dipping structure.

Continental Moho

The arrival at $\simeq$ 3 seconds (labeled *C* on Figures 5.6 through 5.8) is interperted to be a converted wave through the continental Moho. The interface was modeled as a horizontal layer due to the relatively small amplitude of this arrival with respect to the direct *P* wave at most backazimuths. Some *C* arrivals are double-peaked suggesting the addition of a thin layer with a small *S* velocity contrast, however, this complication is not justified by other regional velocity studies and was not resolvable by modeling.

Juan de Fuca Slab

On the radial receiver functions near five seconds, the large negative pulse followed by a large positive arrival indicates a low velocity layer. The negative arrival (labeled *J* in Figures 5.6 through 5.8) is interpreted to be the converted phase from the top of the subducting Juan de Fuca plate and the subsequent large, positive pulse (labeled *O)* from the oceanic Moho. This negative-positive pair of arrivals is observed over a wide range of backazimuths. The amplitude variations

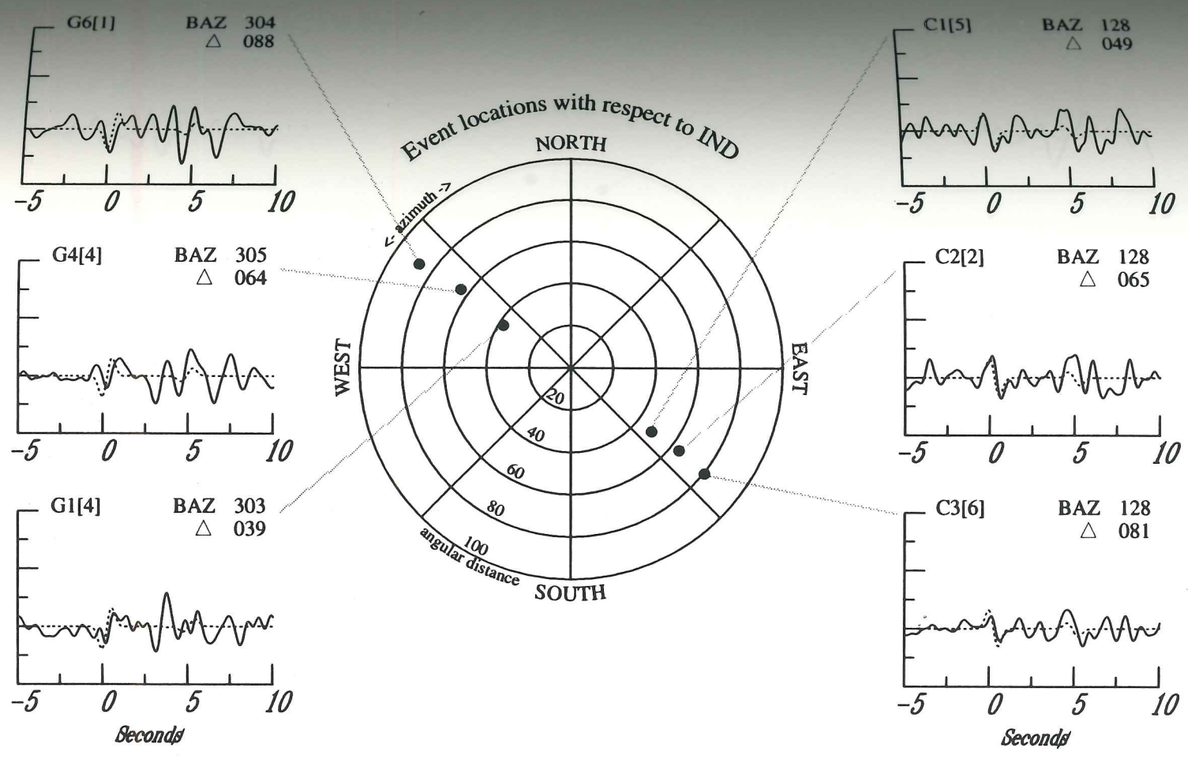

Figure 5.9 Tangential observed (solid) and synthetic (dashed) receiver functions at a range of backazimuths and distances for lithospheric model illustrated in Figure 5.5.

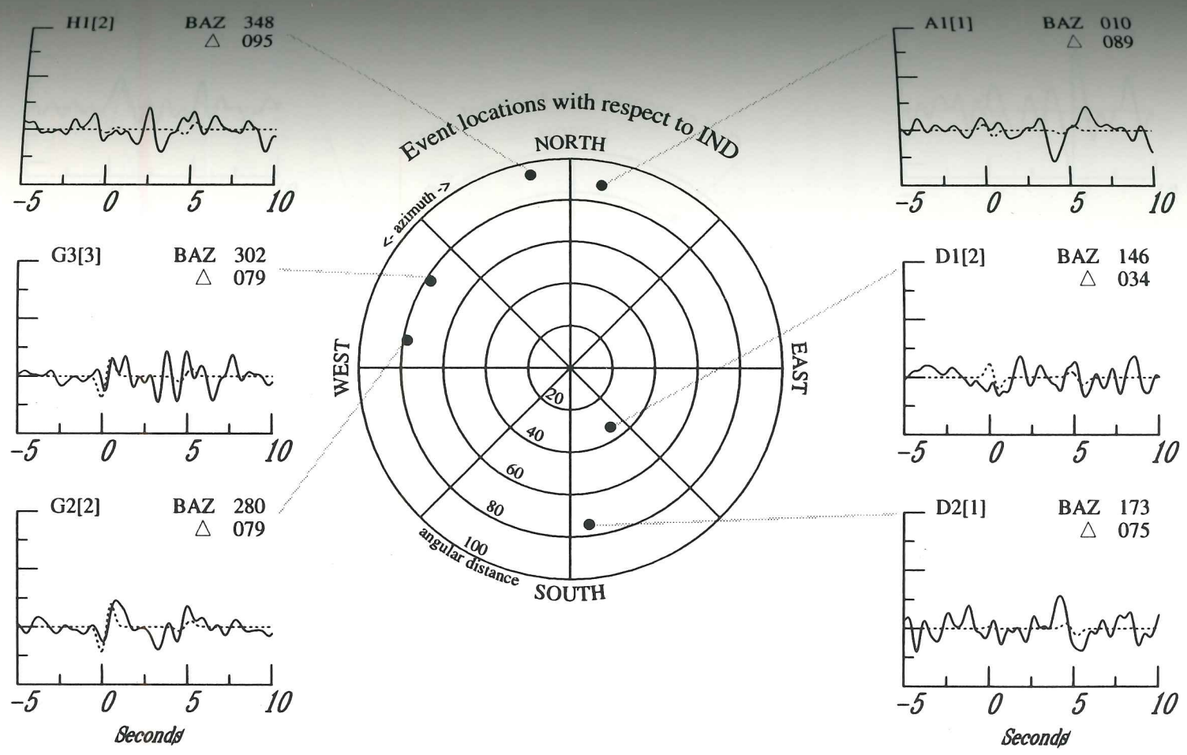

Figure 5.10 Tangential observed (solid) and synthetic (dashed) receiver function at a range of backazimuths and distances for lithospheric model illustrated in Figure 5.5.

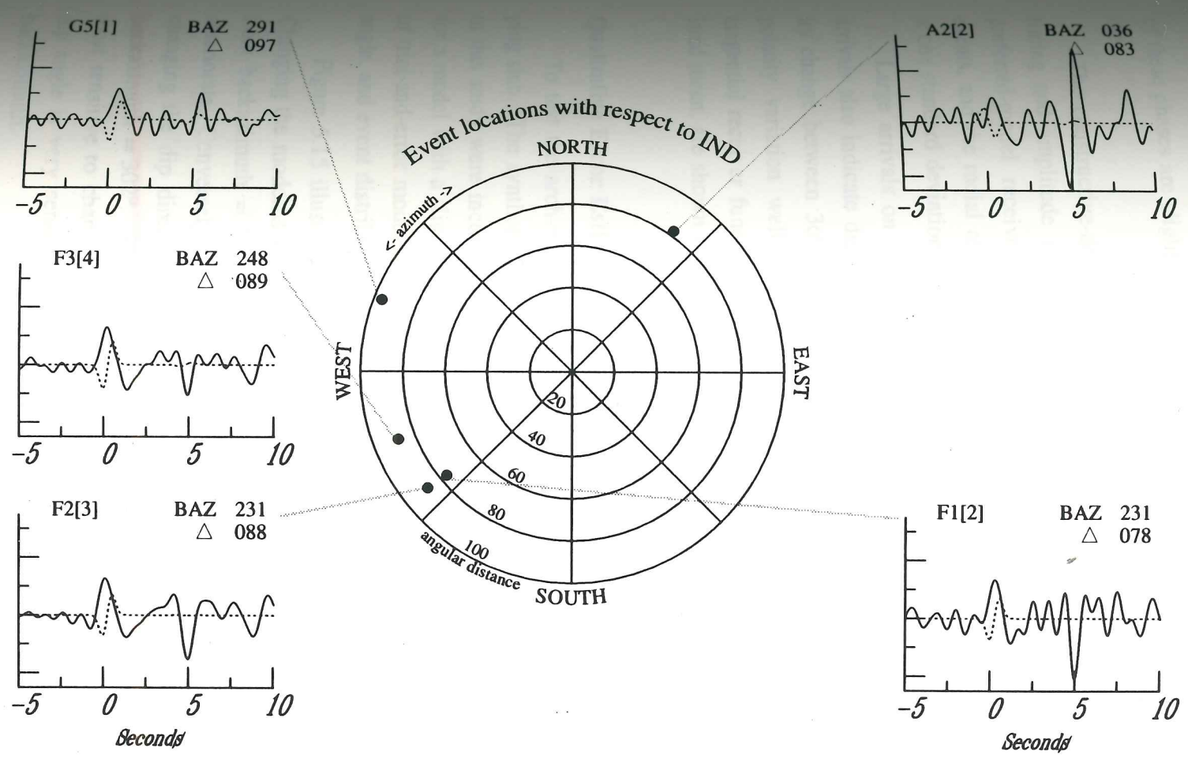

Figure 5.11 Tangential observed (solid) and synthetic (dashed) receiver functions at a range of backazimuths and distances for lithospheric model illustrated in Figure 5.5.

of these phases are slight over the wide range of backazimuths, indicating a shallow dip.

The constructive-destructive influence of reverberations can be seen on the timing and amplitude fits to this pair from some backazimuths. The fits to the preferred-model receiver functions are consistent with the majority of stacked events, and the radial receiver functions generated from this model are compared to ± one standard deviation from the calculated mean in Figures 5.12 through 5.14.

Large arrivals on the tangential components corresponding to the $J-O$ phase arrivals also indicate dipping or complex structure. In the synthetic data the polarity change between 36° and 130° predicted by the modeled slab fits the observed polarity variation well; supporting the interpretation of a northeastly dip. The tangential receiver functions, compared to ± one standard deviation from the calculated mean, are shown in Figures 5.16 through 5.18.

Qualitative Error Estimation

To test the arch-model hypothesis we first modeled the subcrust with no dipping slab. The synthetic fit to the events from the wide range of azimuths available in this study were incompatible with this interpretation. Fits improved substantially for a model with a slightly northeast-dipping slab. The preferred model is the result of trial-and-error modeling and analysis of the trade offs between dip direction, dip angle, and event distribution.

Figure 5.15 illustrates the qualitative bounds determined for the dip direction. Changing the modeled slab dip direction to $N\ 20^{o}\ E$ improves the match for events from backazimuth = 302°, however, the fits to events from backazimuth = 128° deteriorate. Conversely, improving the fit for events from backazimuth = 128 by changing the dip direction to $N\ 80^{o}\ E$ substantially reduces the amplitudes from backazimuth = 302°. The event stacks from the northwest and southeast are the most sensitive to changes in dip direction. Within the dip direction constraints the dip angle is very sensitive, and dips ≥ 12° are not consistent with data from any backazimuth.

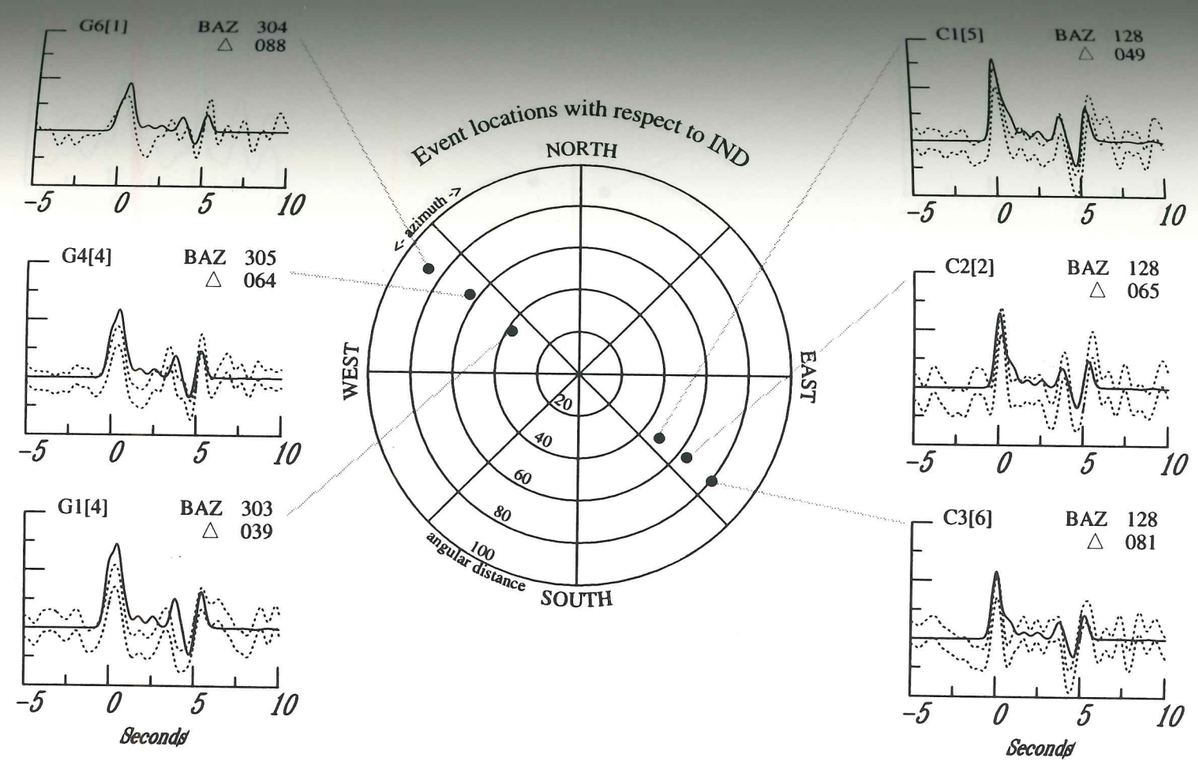

Figure 5.12 Synthetic radial receiver functions (solid) compared to +/- one standard deviation to the calculated mean (dashed). Receiver functions with one event are shown as a single line.

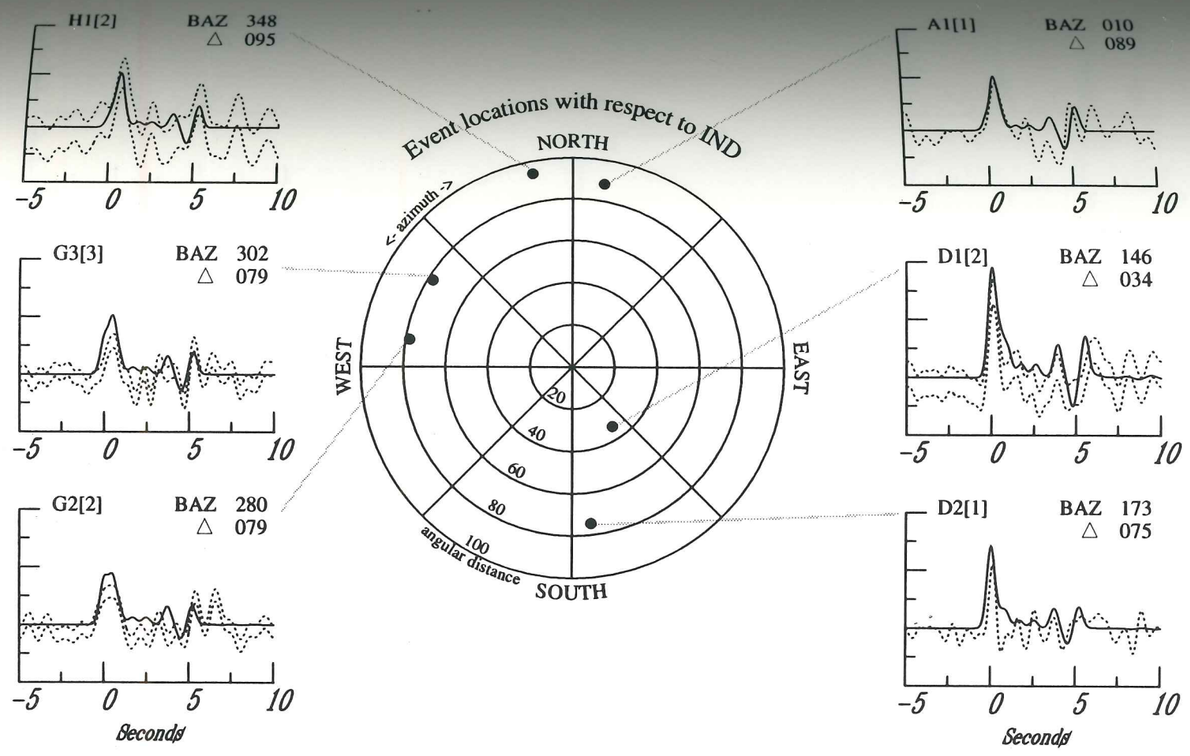

Figure 5.13 Synthetic radial receiver functions (solid) compared to +/- one standard deviation to the calculated mean (dashed). Receiver functions with one event are shown as a single line.

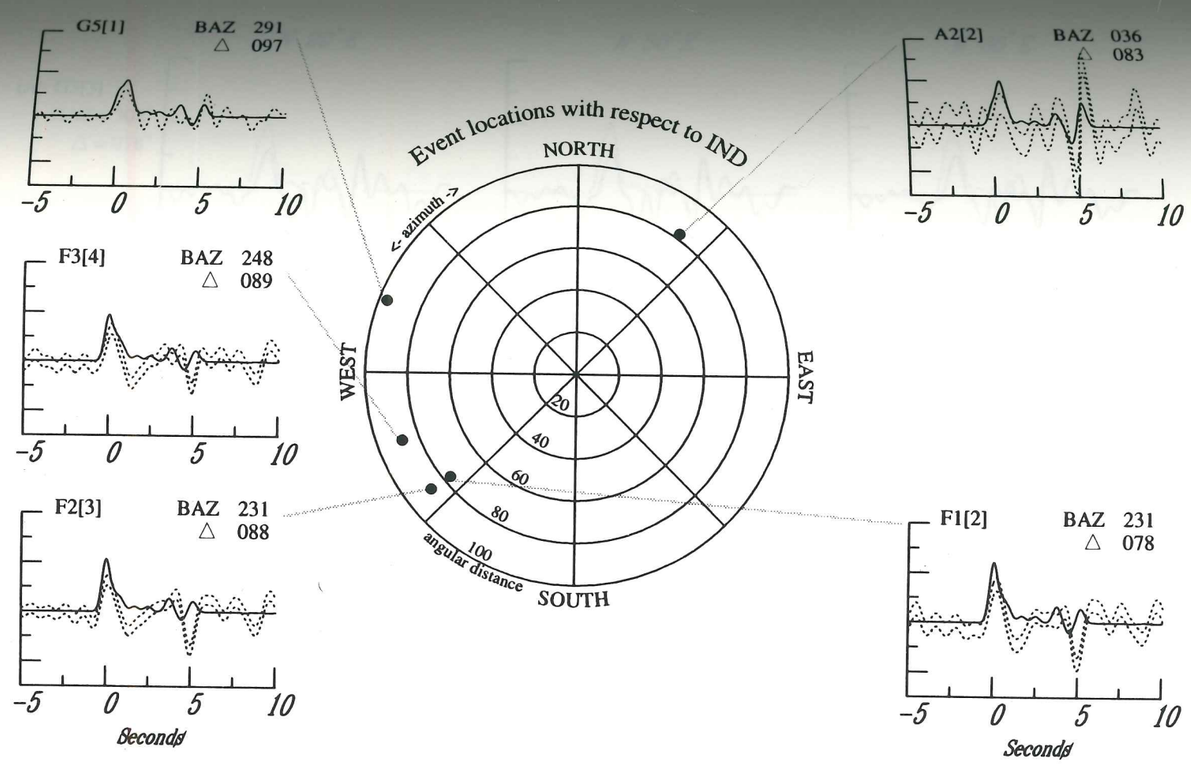

Figure 5.14 Synthetic radial receiver functions (solid) compared to +/- one standard deviation to the calculated mean (dashed). Receiver functions with one event are shown as a single line.

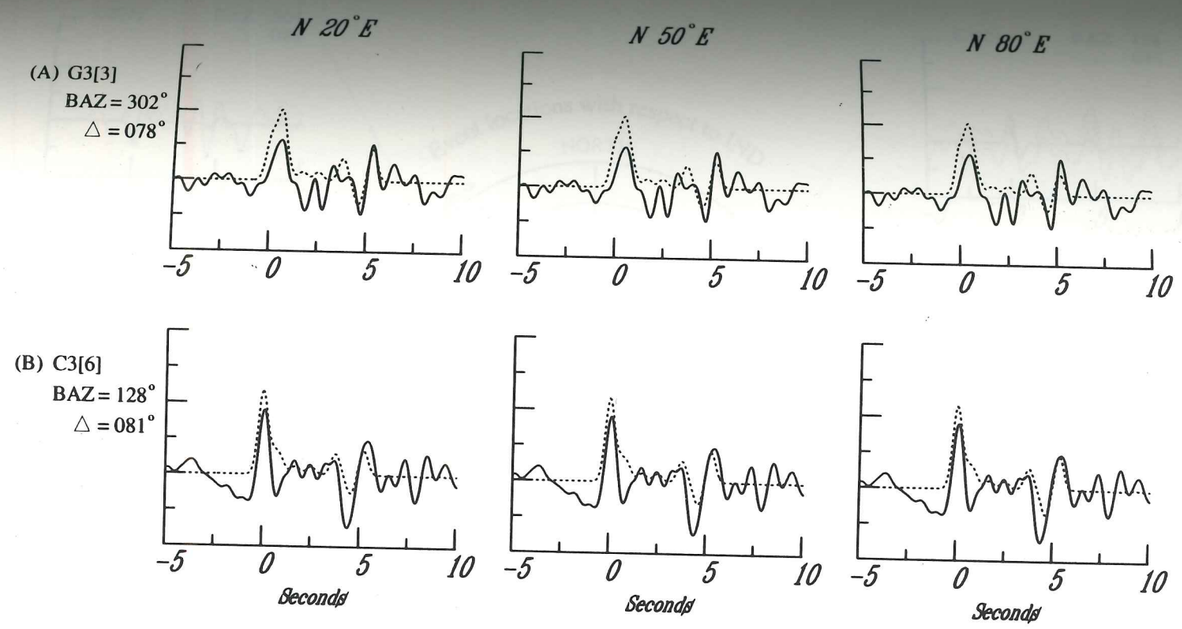

Figure 5.15 Oceanic Moho dip direction analysis for events from two backazimuths. (A) best-fit model dip direction = N 20 E for backazimuth = 302 degrees, (B) best-fit model dip direction = N 80 E for backazimuth = 128 degrees. Preferred model dip direction = N 50 E.

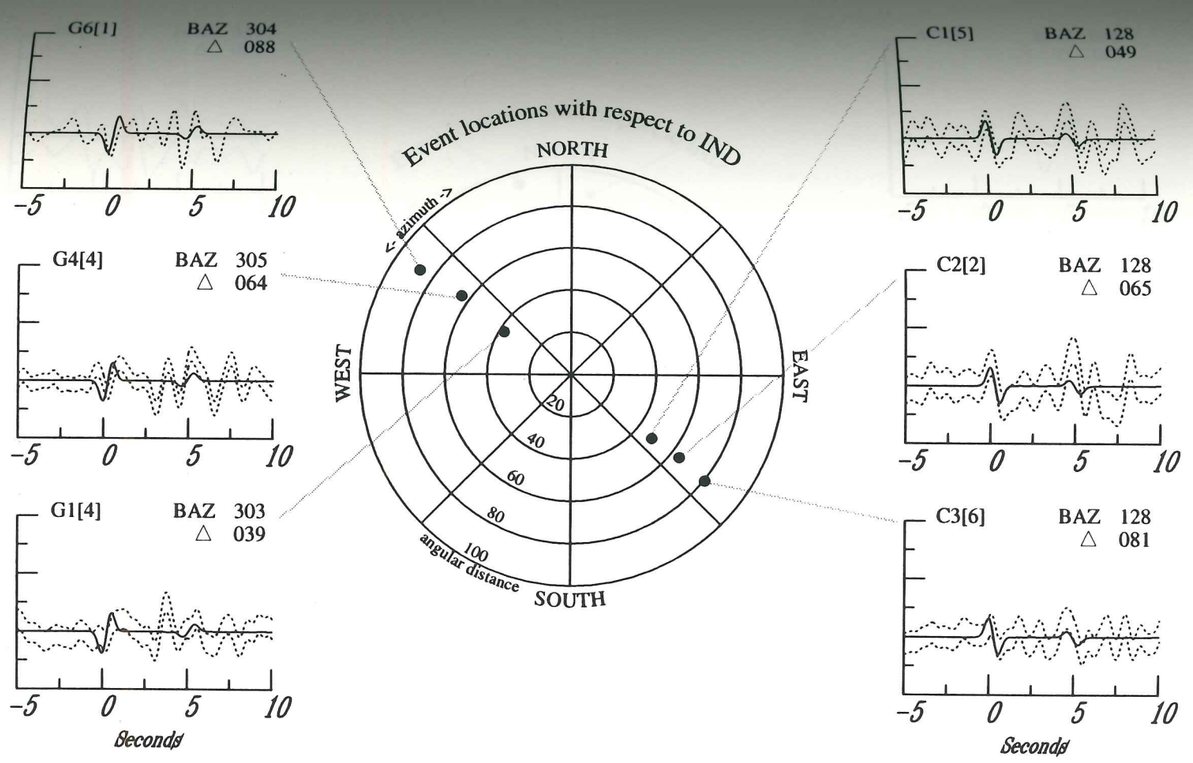

Figure 5.16 Synthetic tangential receiver functions (solid) compared to +/- one standard deviation to the calculated mean (dashed). Receiver functions with one event are shown as a single line.

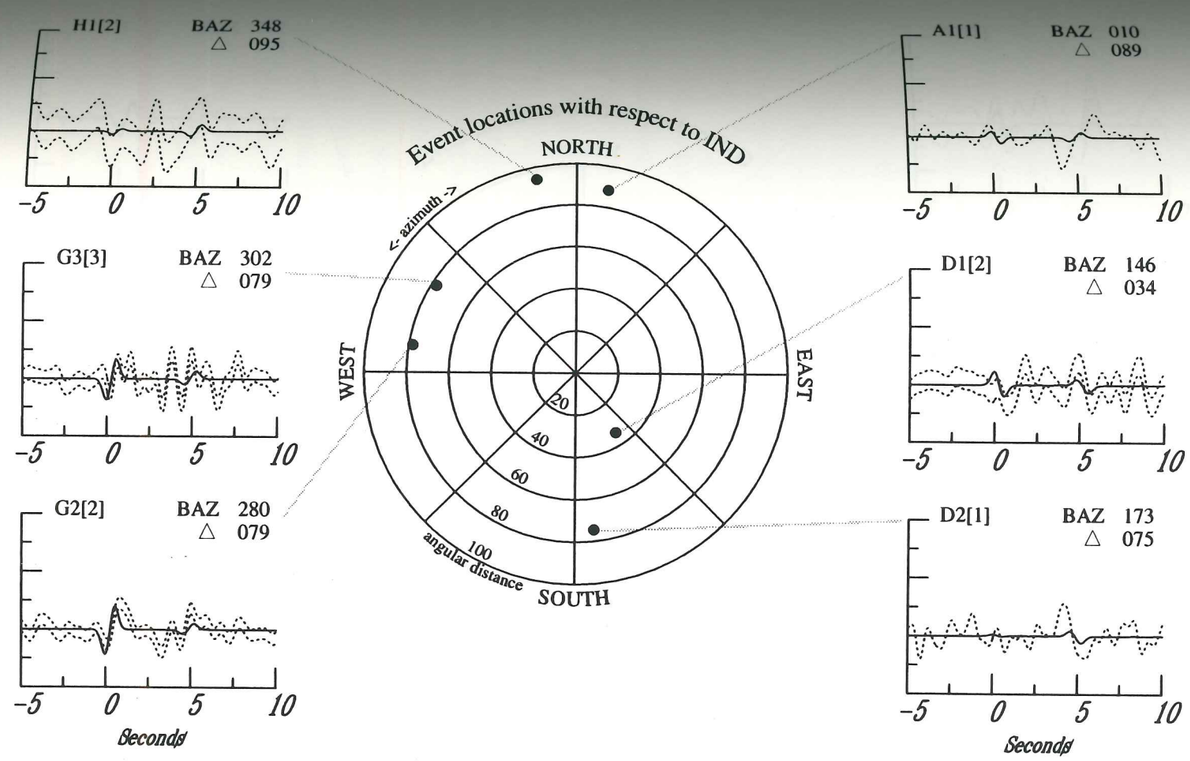

Figure 5.17 Synthetic tangential receiver functions (solid) compared to +/- one standard deviation to the calculated mean (dashed). Receiver functions with one event are shown as a single line.

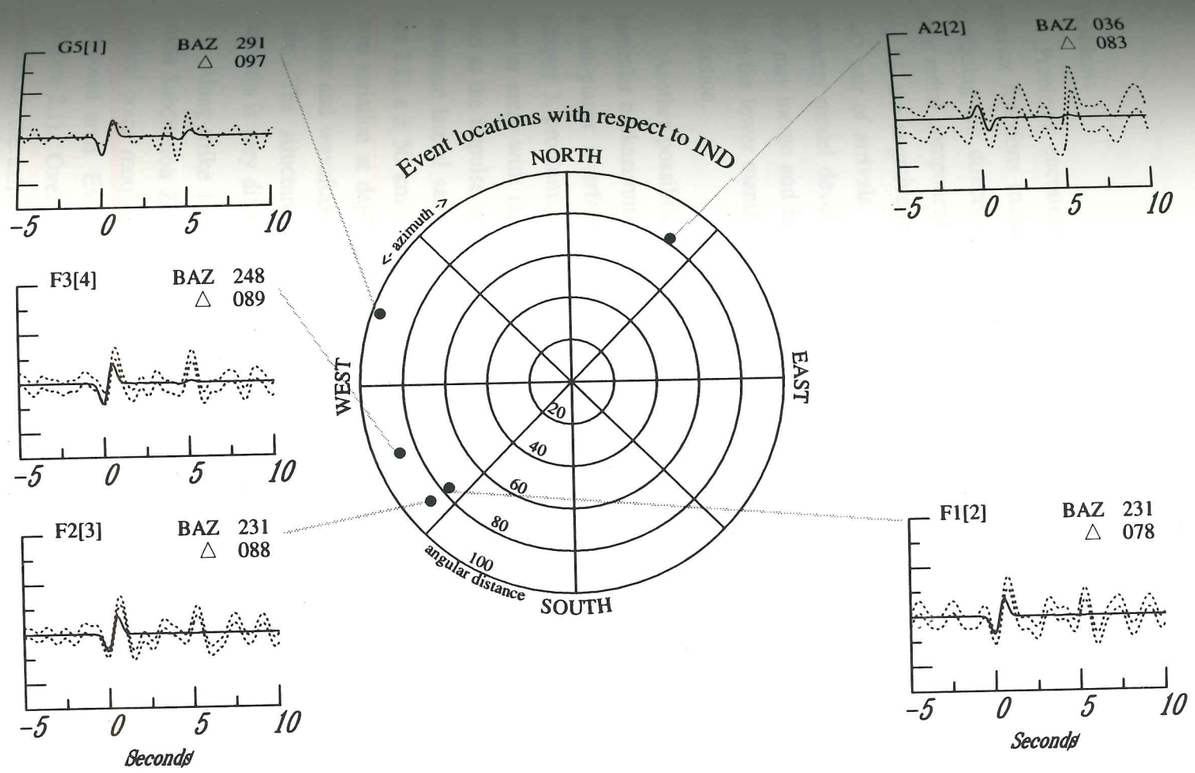

Figure 5.18 Synthetic tangential receiver functions (solid) compared to +/- one standard deviation to the calculated mean (dashed). Receiver functions with one event are shown as a single line.

Problems

Problems encountered during forward modeling of the radial and tangential receiver functions include observations of time delayed phase arrivals, apparently conflicting dip directions, and anomalously large amplitudes on the tangential and some radial components. On each of the event stacks from the southwest: *F1*, *F2*, and *F3*, the negative-to-positive pulse arrives much too late to be modeled as the *J–O* pair of arrivals. These huge time shifts can not be explained by the simple-geometry model developed in this study. Beyond about backazimuth = 85°, *P* and *PcP* may merge and become core grazing phases. It is possible that some complexity in the lower mantle may also affect the receiver functions by distoring the particle motion.

Another possibility is that local anisotropy could play a role in affecting those particular backazimuths. The time variations may represent lateral variations due to a non-planar interface or lateral velocity variation beneath IND. As noted in Chapter 3, problems due to lateral sampling may occur in areas of complex structure or areas with rapidly varying velocities. Approximation of the receiver function as the impulse response directly beneath the station requires the assumption of minimum lateral sampling. In cross-section view (see middle cross-section in Figure 2.2), a ± 50 km area on either side of the station encompasses very large structural variation at depth. The pinchout of the asthenospheric wedge is updip of this station and waveforms arriving from the SW will sample this very complex structure. The structure of the asthenosphere encountered by arrivals from other azimuths is very different and much less complex.

Along-strike lateral variations are expected to occur in this area of the Cascadia Subduction Zone. The need to define the slab dip direction and angle at this critical point motivated the positioning of the recording site near the apex of the proposed arch. Evidence of along-strike heterogeneity can be seen in map view (Figure 2.1). Over a 50 km radius (the approximate depth to the deepest reflecting interface), the azimuths of the arch contours change drastically, from ≈ *N* 45° *W* to ≈ due *N*. This heterogeneity may be the primary reason events from the *NW* and

SE yield apparently conflicting slab dip-direction results, and is consistent with waveforms sampling a near-apex arch structure.

The observed transverse component arrivals are often as large or larger than the corresponding arrivals on the radial component which also indicates very complex, inhomogeneous structure. Although the timing and polarity of the modeled arrivals is consistent, the large amplitudes cannot be accounted for with this simple geometric model. On the radial receiver functions, the amplitudes of the *J–O* arrival pair is often up to two times as large as the first arriving energy; this large an amplitude on a converted phase can not be explained by a reverberation from laterally inhomogeneous structure alone. The observed signals from the northeast: A2, have extremely large amplitude *J* and *O* arrivals. The effect of multiples generated at the dipping shallow structure was qualitatively modeled as contributing to these anomalously high amplitudes, although this effect is not seen at all backazimuths.

Chapter 6

Discussion

Source equalized teleseismic *P* waveforms were used to determine crustal and upper mantle structure in central Puget Sound. Despite lateral complexities beneath IND, *P-to-S* converted arrivals corresponding to the shallow structure, the continental Moho, and the subducting Juan de Fuca slab were successfully modeled, providing several new pieces of information on the earth structure beneath IND.

Table 6.1 summarizes the results of this study for the major features modeled in the subcrust, and lists the results from two other studies in the region for comparison. The bottom of the crust as well as the depth to the oceanic Moho beneath IND are shallower than those depths obtained from receiver function studies to the north [*Cassidy* 1991] and south [*Lapp et al* 1990]. The slab also has a relatively shallower dip in this area of the Cascadia subduction zone. The estimated uncertainties for the parameters modeled in this study are:

North American Plate:

Continental Moho depth: 28.9 km ± 1.0 km

Juan de Fuca Plate:

Oceanic Moho depth: 43.4 km ± 1.0 km

Oceanic crust dip direction: $N\ 50^{o}\ E \pm 30^{o}$

Oceanic crust dip angle: $8^{o} \pm 3^{o}$

The depth to the continental Moho estimated through modeling corresponds to the crust thickness inferred from seismicity of 25-30 km. The shallow slab dip, and depth to the oceanic Moho derived in this study are also consistent with observations made from seismicity (see middle cross-section in Figure 2.2). From seismicity, the dip of and depth to the oceanic Moho are approximated at 10^{o} and 40-45 km, respectively.

The parameters obtained in this study for the JDF slab are consistent with the arch model of *Crosson and Owens* [1987] which predicted a shallow, northeastly slab dip and a depth to the oceanic Moho of approximately 45 km. The large uncertainty in the strike direction is caused by along strike heterogeneity near the crest of the arch where the dip direction sweeps through a 45^{o} angle within a 50 km

Table 6.1

Comparison of Structural Parameters					
	Lapp et al [1990]	Indian Island	*Cassidy* [1991] ALB	LAS	EGM
Latitude	46.8 N	48.0 N	49.3 N	49.5 N	49.8 N
Longitude	122.7 W	122.7 W	124.9 W	124.2 W	123.9 W
Depth of CM	31 km	29 km	-	37 km	36 km
Depth of OM	54 km	43 km	50 km	60 km	70 km
JDF Strike	N 35 E	N 40 W	N 30 W	N 30 W	N 30 W
JDF Dip	16	8	15	10	15

radius of the recording sight, i.e. waveforms sample the arch in a region where the dip is changing rapidly. Reverberations from deep structure which is very different up- and down-dip also complicate the waveforms.

The local structure beneath IND is very complex and the geometric parameters obtained in this study have improved our knowledge of the JDF plate geometry as well as the crustal structure. Ongoing studies north and south of this recording site will certainly further illuminate the slab structure and may help explain the complex signals observed in this study.

Bibliography

Ammon, C.J., G.E. Randall , and G. Zandt (1990). On the nonuniquenss of receiver function inversion, *J. Geophys. Res.*, **95**, 15,303-15,318.

Atwater, B.F. (1987). Evidence for great holocene earthquakes along the outer coast of Washington State, *Science,* **236**, 942-944.

Cassidy, J.F. (1991). *Teleseismic receiver function analysis of the crust and upper mantle of southwestern British Columbia* , Ph.D. dissertation, Univ of British Columbia , Vancouver, 174pp.

Chiao, L.-Y. and K.C. Creager (1989). Kinematic Deformation of the Subducted Cascadia Slab (abstract), *EOS,* **70** , 1328.

Crosson, R.S. (1983). Review of seismicity in the Puget Sound region from 1970 through 1978, in *Proceedings of Workshop XIV, Earthquake Hazards of the Puget Sound Region,Washington, USGS Open File Rept. 83-19,* edited by J.C. Yount and R.S. Crosson, U.S. Geol. Survey, 6-18.

Crosson, R.S. and T.J. Owens (1987). Slab geometry of the Cascadia subduction zone beneath Washington from earthquake hypocenters and teleseismic converted waves, *Geophys. Res. Letts.*, **14**, 824-827.

Davis, E.E. and R.D. Hyndman (1989). Accretion and recent deformation of sediments along the northern Cascadia subduction zone, *Geol. Soc. Am. Bull.*, **101**, 1465-1480.

Dickinson, W.R. (1970). Relations of andesites, granites, and derivative sandstones to arc-trench tectonics, *Rev. Geophys.*, **8**, 813-860.

Heaton, T.H. and P.D. Snavely (1985). Possible tsunami along the northwestern coast of the United States inferred from Indian traditions, *Bull. Seis. Soc. Am.*, **75**, 1455-1460.

Heaton, T.H. and S.H. Hartzell (1987). Earthquake hazards on the Cascadia subduction zone, *Science,* **236**, 162-168.

Heaton, T. H. (1990). The calm before the quake?, *Science,* **343**, 511.

Helmberger, D. and R.A. Wiggins (1971). Upper mantle structure of the Midwestern United States, *J. Geophys. Res.*, **76**, 3229-3245.

Hendrickson, M.A. (1986). *The determination of seismic structure from teleseismic P waveforms on the Washington continental margin,* M.S. Thesis, Univ. of Washington, Seattle, 74 pp.

Langston, C.A. (1977). The effect of planar dipping structure on source and receiver responses for constant ray parameter, *Bull. Seis. Soc. Am.*, **67**, 1029-1050.

Langston, C.A. (1979). Structure under Mount Rainier, Washington, inferred from teleseismic body waves, *J. Geophys. Res.*, **84**, 4749-4762.

Lapp, D.B. (1987). *The subduction geometry beneath western Washington from deconvolved teleseismic P-waveforms,* M.S. Thesis, Univ. of Washington, Seattle, 70 pp.

Lapp, D.B., T.J. Owens, and R.S. Crosson (1990). P-waveform analysis for local subduction geometry south of Puget Sound, Washington, *Pageoph,* **133**, 349-365.

Owens, T.J., S.R. Taylor, and G. Zandt (1983a). Isolation and enhancement of the response of local seismic structure from teleseismic P-waveforms, *UCID-19809,* Lawrence Livermore Laboratory.

Owens, T.J., S.R. Taylor, and G. Zandt (1983b). Crustal structure beneath RSTN stations inferred from teleseismic P-waveforms: preliminary results at RSCP, RSSD, and RSNY, *UCID-19859,* Lawrence Livermore Laboratory.

Owens, T.J., R.S. Crosson, and M.A. Hendrickson (1988). Constraints on the subduction geometry beneath western Washington from broadband teleseismic waveform modeling, *Bull. Seis. Soc. Am.*, **78**, 1319-1334.

Owens, T.J. and R.S. Crosson (1988). Shallow structure effects on broadband teleseismic P-waveforms, *Bull. Seis. Soc. Am.*, **78**, 96-108.

Pessel, F. Jr., D.P. Dethier, D.B. Booth, and J.P. Minard (1989). Surficial Geologic

Map of the Port Townsend 30- by 60-Minute Quadrangle, Puget Sound Region, Washington, *Map I-1198-F,* Dept. of Interior, U.S. Geological Survey.

Riddihough, R.P. (1984). Recent movements of the Juan de Fuca plate system, *J. Geophys. Res.*, **89**, 6980-6994.

Swann, J.G. (1868). The Indians of Cape Flattery, at the entrance to the straight of Juan de Fuca, Washington Territory, *Smithsonian Contributions to Knowledge,* **220**, 108pp.

Taber, J.J. and S.W. Smith (1985). Seismicity and focal mechanisms associated with the subduction of the Juan de Fuca plate beneath the Olympic Peninsula, Washington, *Bull. Seismol. Soc. Amer.*, **75**, 237-249.

Taber, J.J. and B.T.R. Lewis (1986). Crustal structure of the Washington continental margin from refraction data, *Bull. Seismol. Soc. Amer.*, **76**, 1011-1024.

Tabor, R.W. and W.M. Cady (1978). Geologic map of the Olympic Peninsula, scale 1:125,000, *Misc. Invest. Map I-994,* U.S. Geol. Surv., Reston, Va.

Walters, Anna Lee (1975). 'Come, My Sons', in *The Man to Send Rainclouds,* edited by Kenneth Rosen, New York: Vintage Books, pp 15-26.

Weaver, C.S. and G.E. Baker (1988). Geometry of the Juan de Fuca plate beneath Washington and northern Oregon from seismicity, *Bull. Seis. Soc. Am.*, **78**, 264-275.

Zervas, C.E. and R.S. Crosson (1986). Pn observations and interpretations in Washington, *Bull. Seis. Soc. Am.*, **76**, 521-546.

Appendix A

Receiver Function Stacking Suites

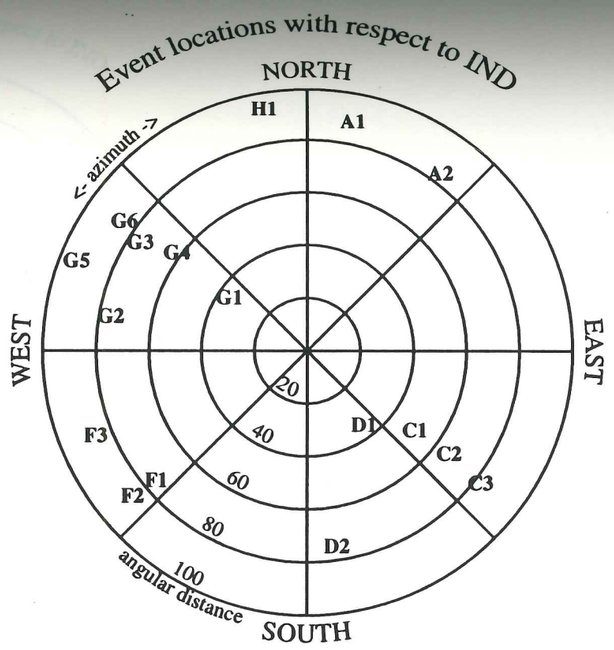

Figure A.1 Location identification codes of stacked and single events used in this study.

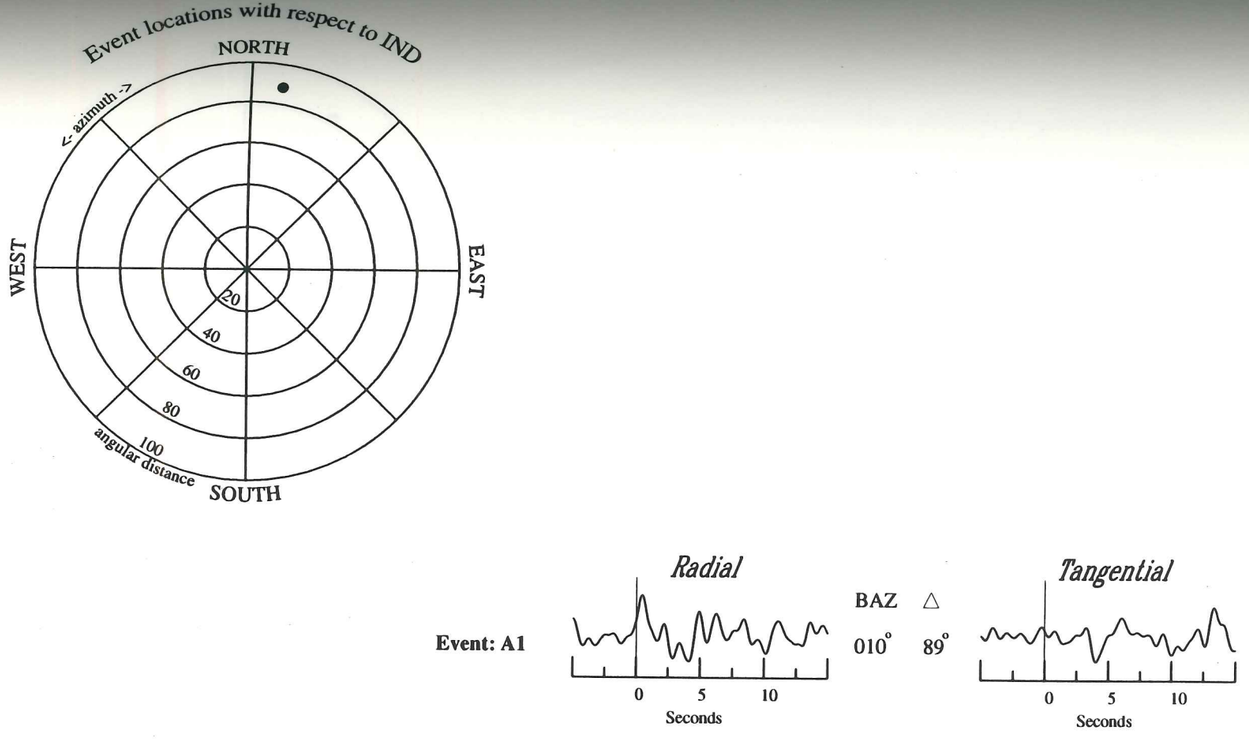

Figure A.2 Event location with respect to IND, and radial and tangential receiver functions for event A1.

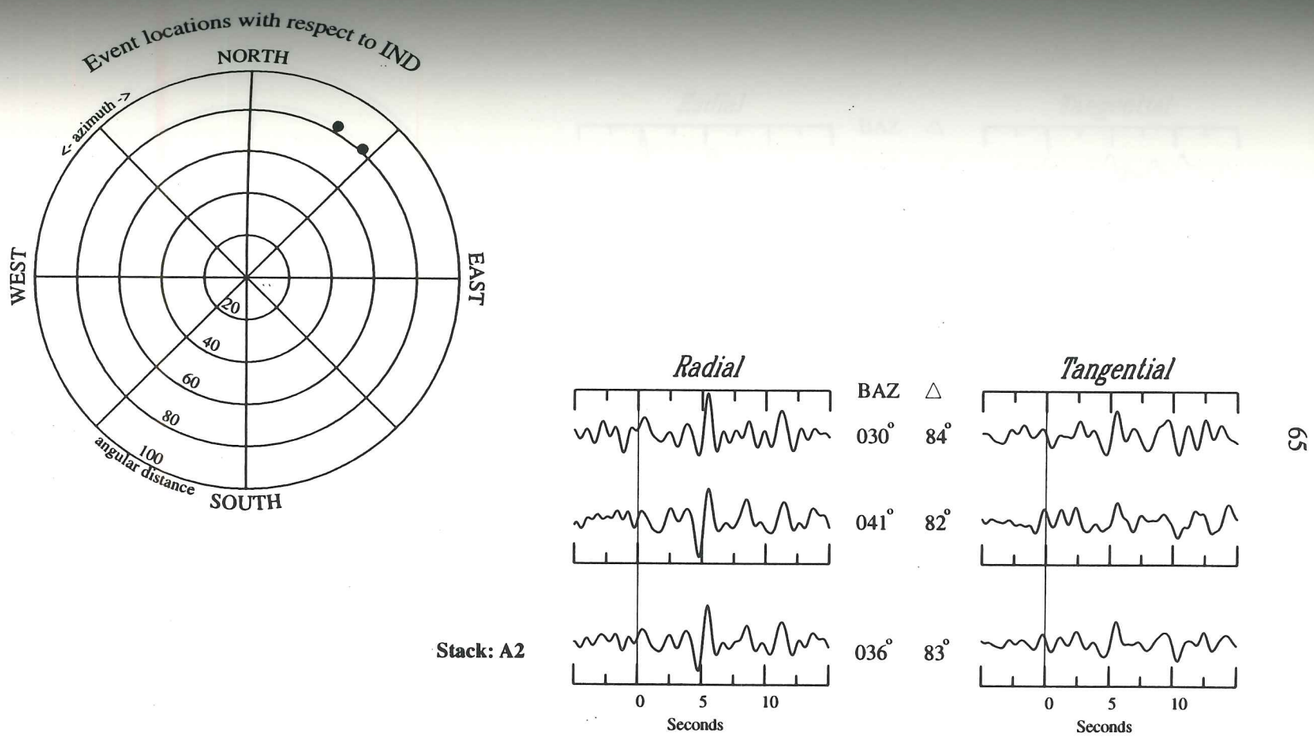

Figure A.3 Event locations with respect to IND, and radial and tangential receiver functions for events in stacking suite A2. Stack backazimuth and distance are averaged from events in the stack.

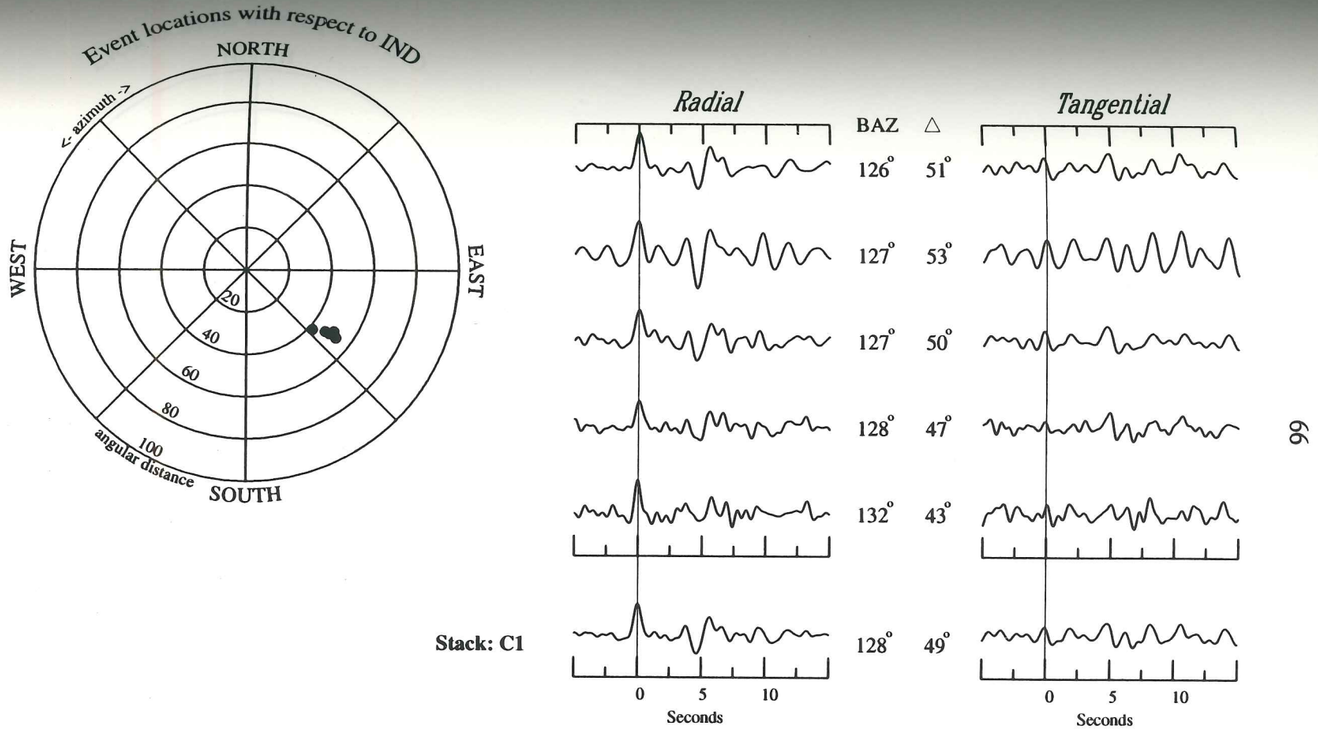

Figure A.4 Event locations with respect to IND, and radial and tangential receiver functions for events in stacking suite C1. Stack backazimuth and distance are averaged from events in the stack.

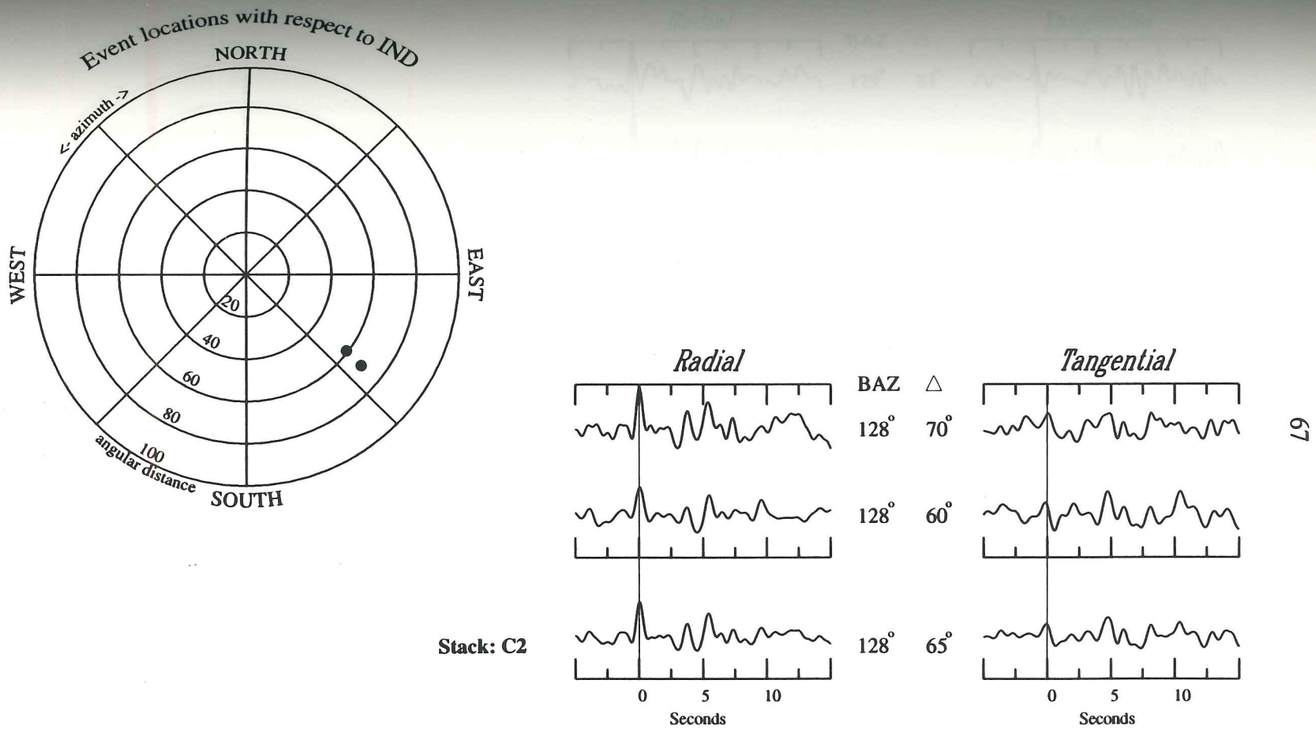

Figure A.5 Event locations with respect to IND, and radial and tangential receiver functions for events in stacking suite C2. Stack backazimuth and distance are averaged from events in the stack.

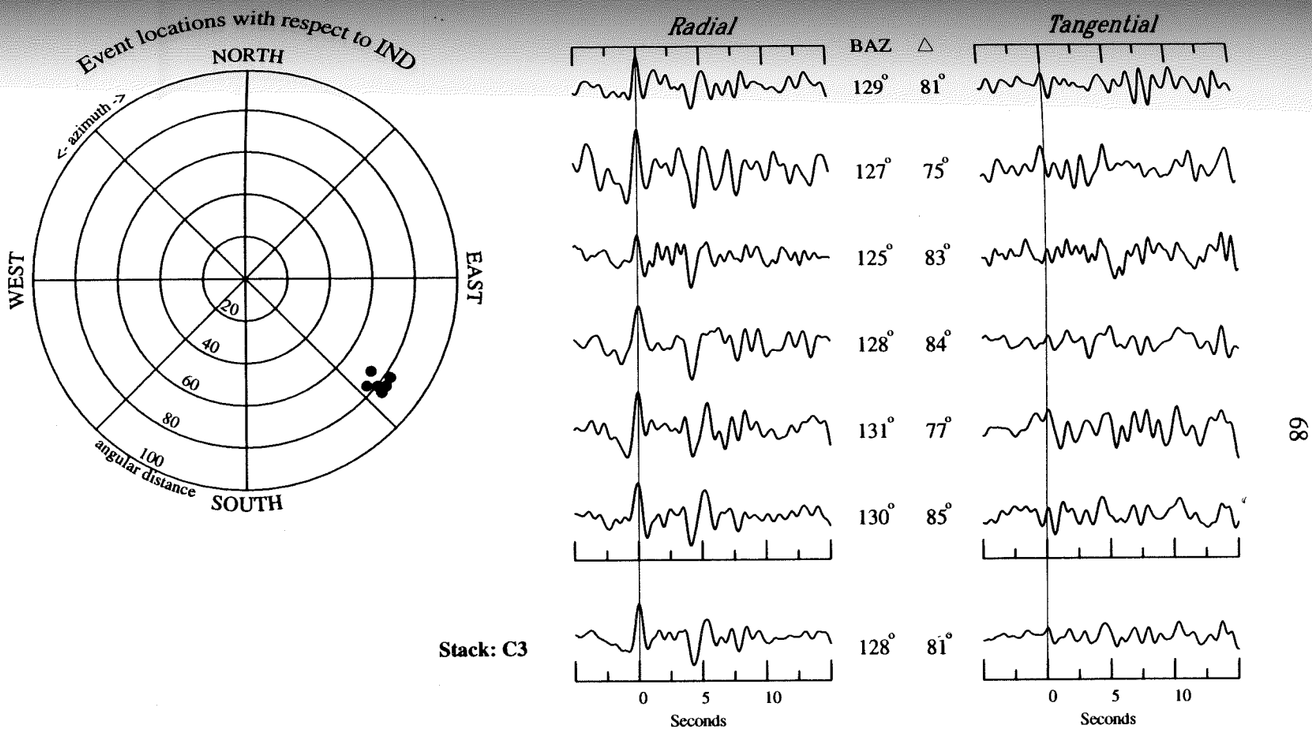

Figure A.6 Event locations with respect to IND, and radial and tangential receiver functions for events in stacking suite C3. Stack backazimuth and distance are averaged from events in the stack.

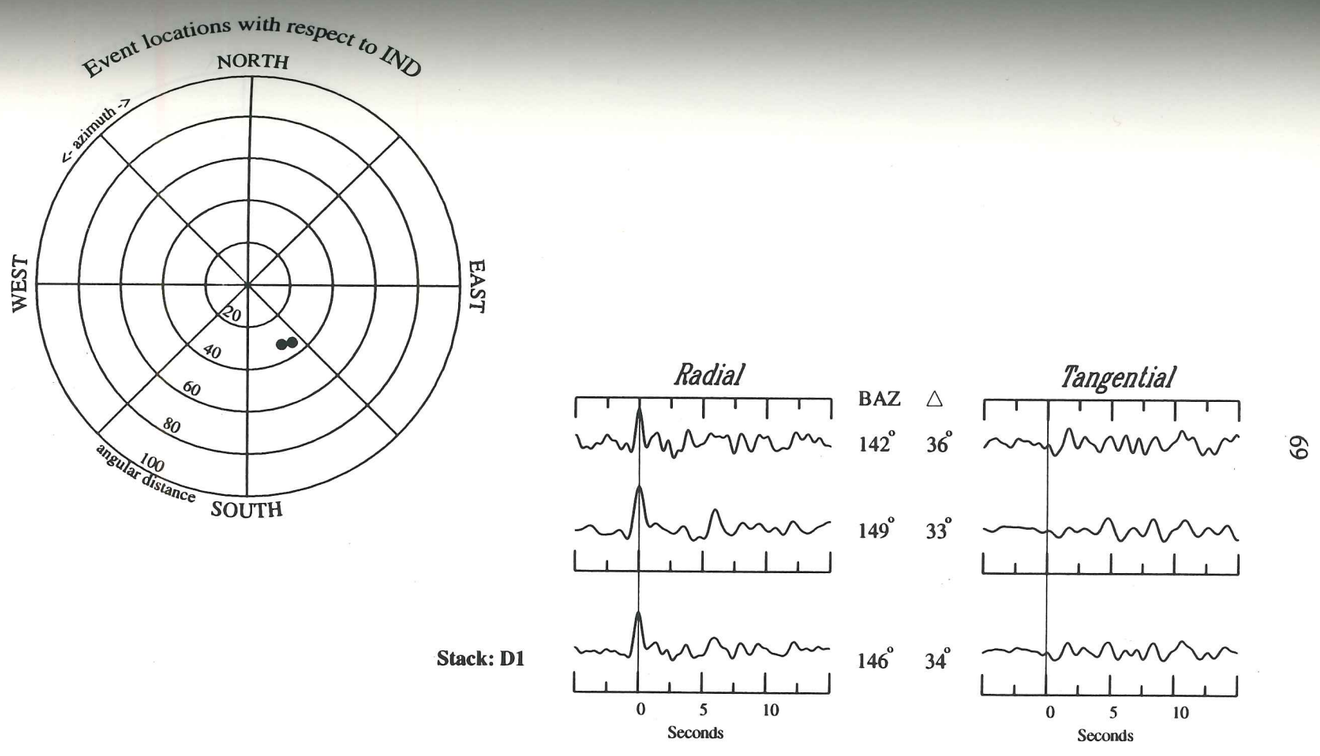

Figure A.7 Event locations with respect to IND, and radial and tangential receiver functions for events in stacking suite D1. Stack backazimuth and distance are averaged from events in the stack.

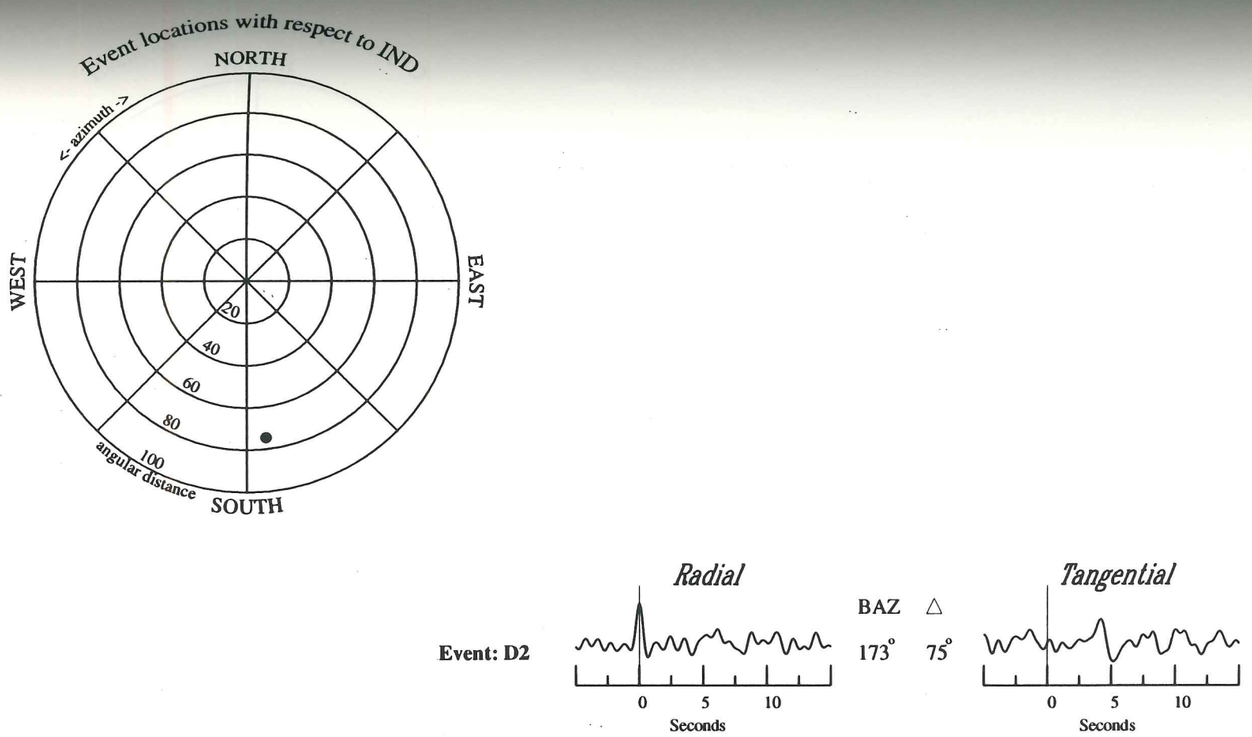

Figure A.8 Event location with respect to IND, and radial and tangential receiver functions for event D2.

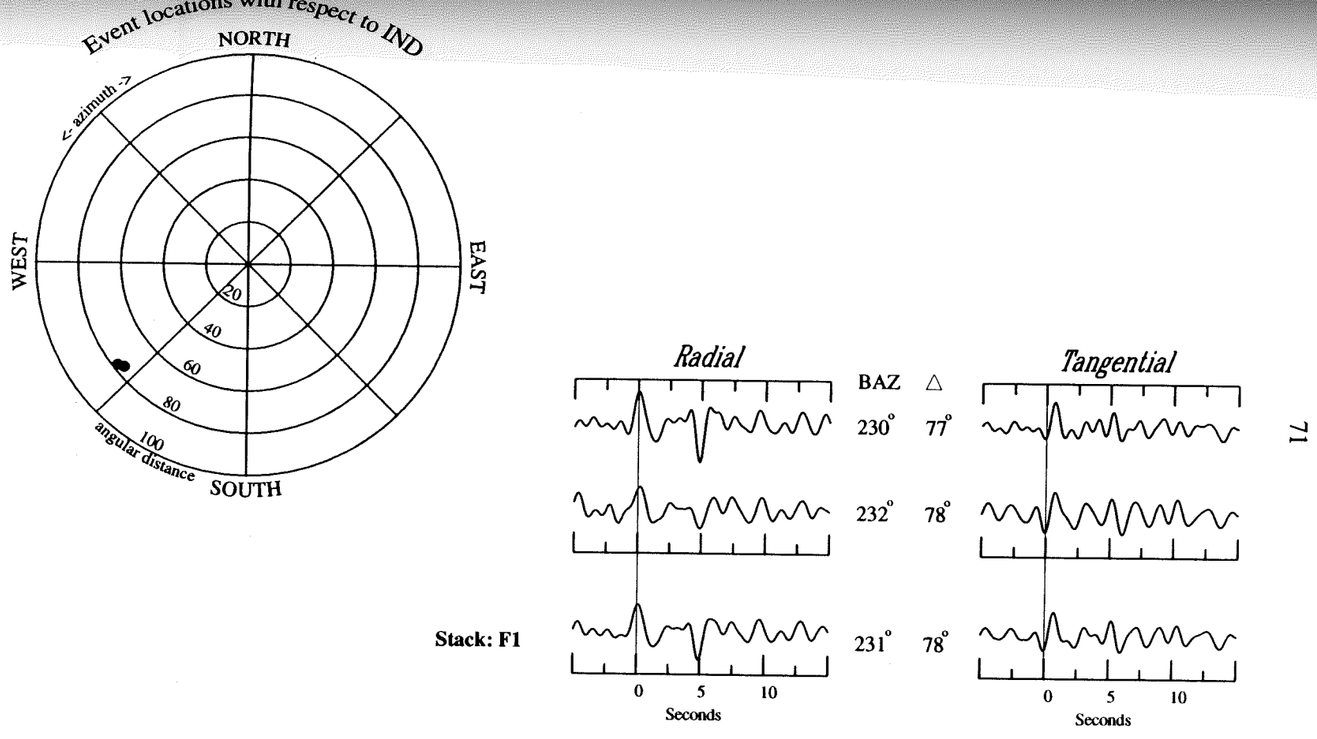

Figure A.9 Event locations with respect to IND, and radial and tangential receiver functions for events in stacking suite F1. Stack backazimuth and distance are averaged from events in the stack.

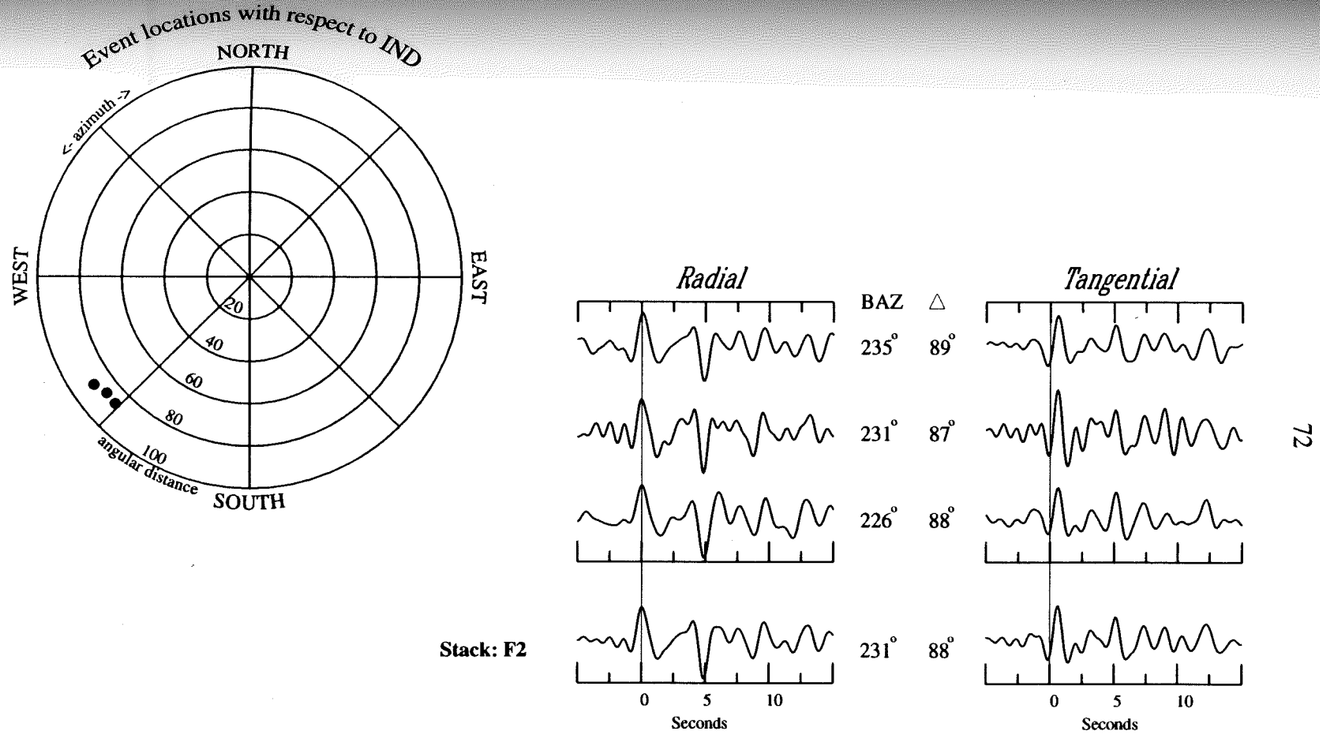

Figure A.10 Event locations with respect to IND, and radial and tangential receiver functions for events in stacking suite F2. Stack backazimuth and distance are averaged from events in the stack.

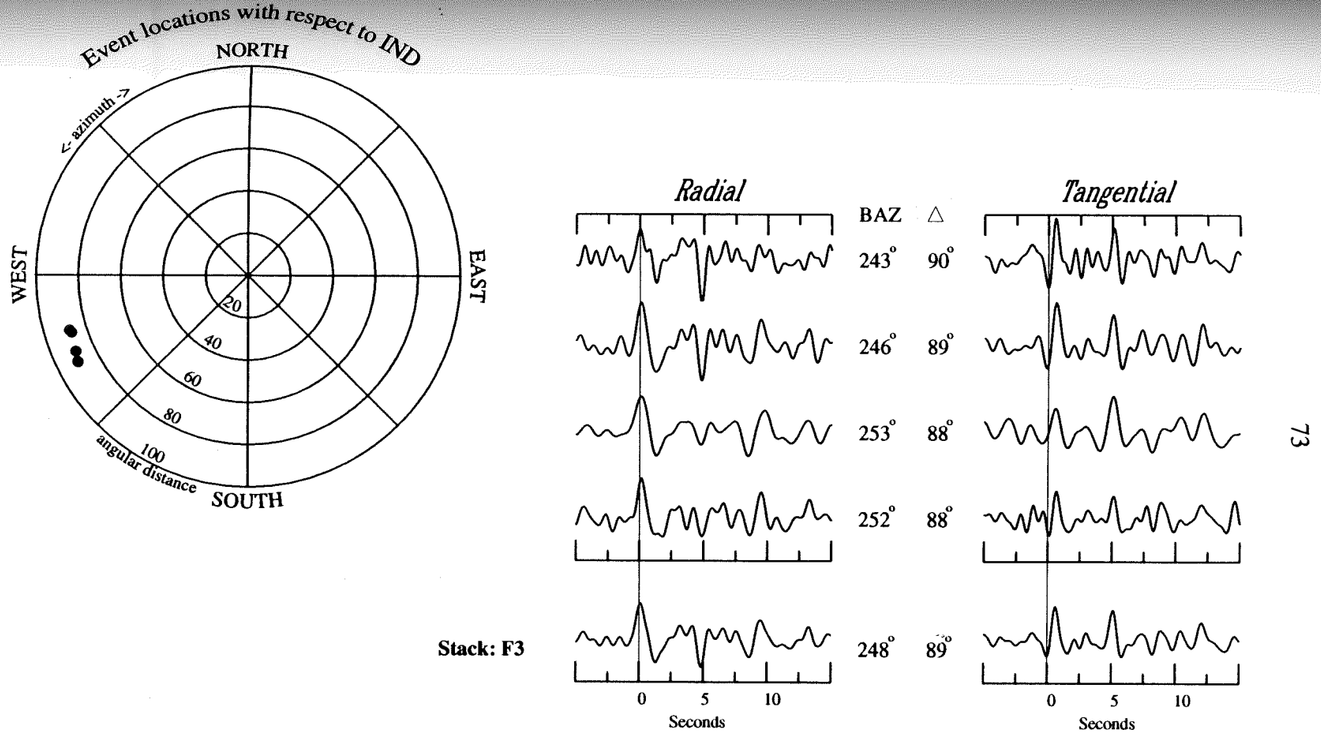

Figure A.11 Event locations with respect to IND, and radial and tangential receiver functions for events in stacking suite F3. Stack backazimuth and distance are averaged from events in the stack.

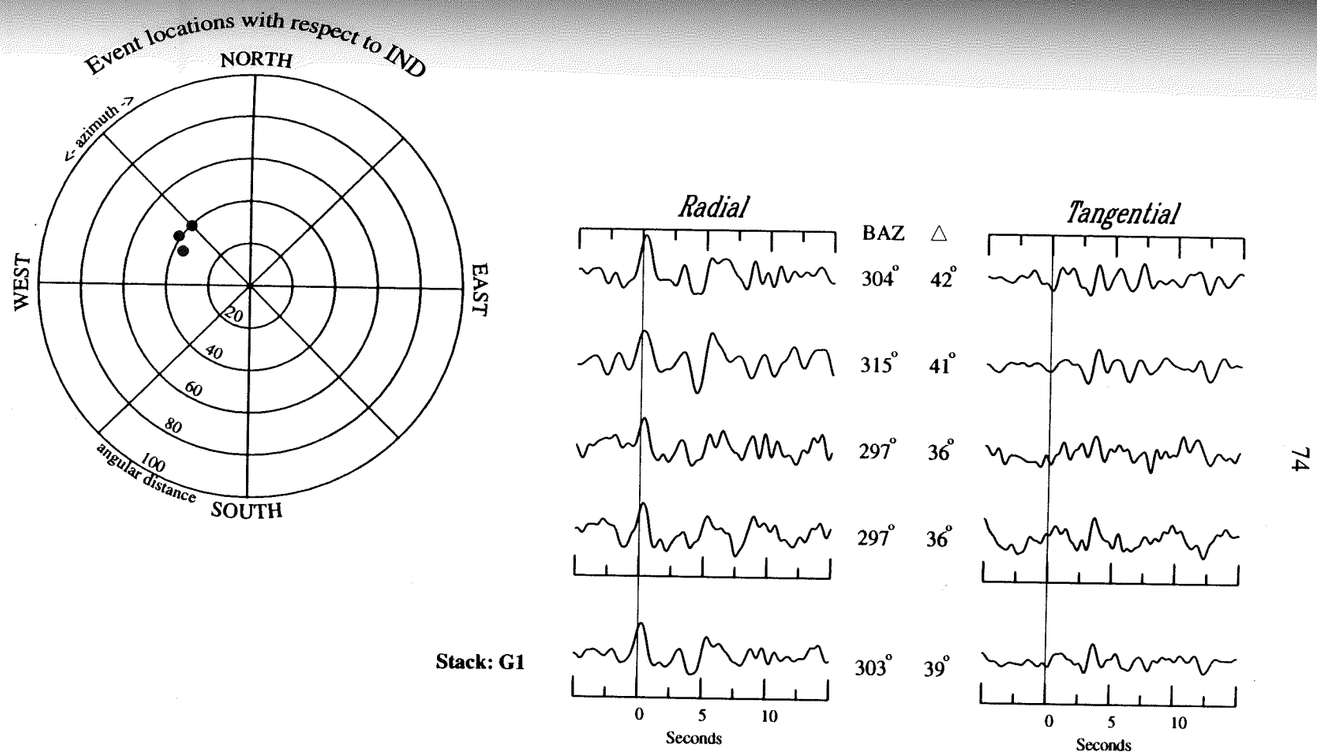

Figure A.12 Event locations with respect to IND, and radial and tangential receiver functions for events in stacking suite G1. Stack backazimuth and distance are averaged from events in the stack.

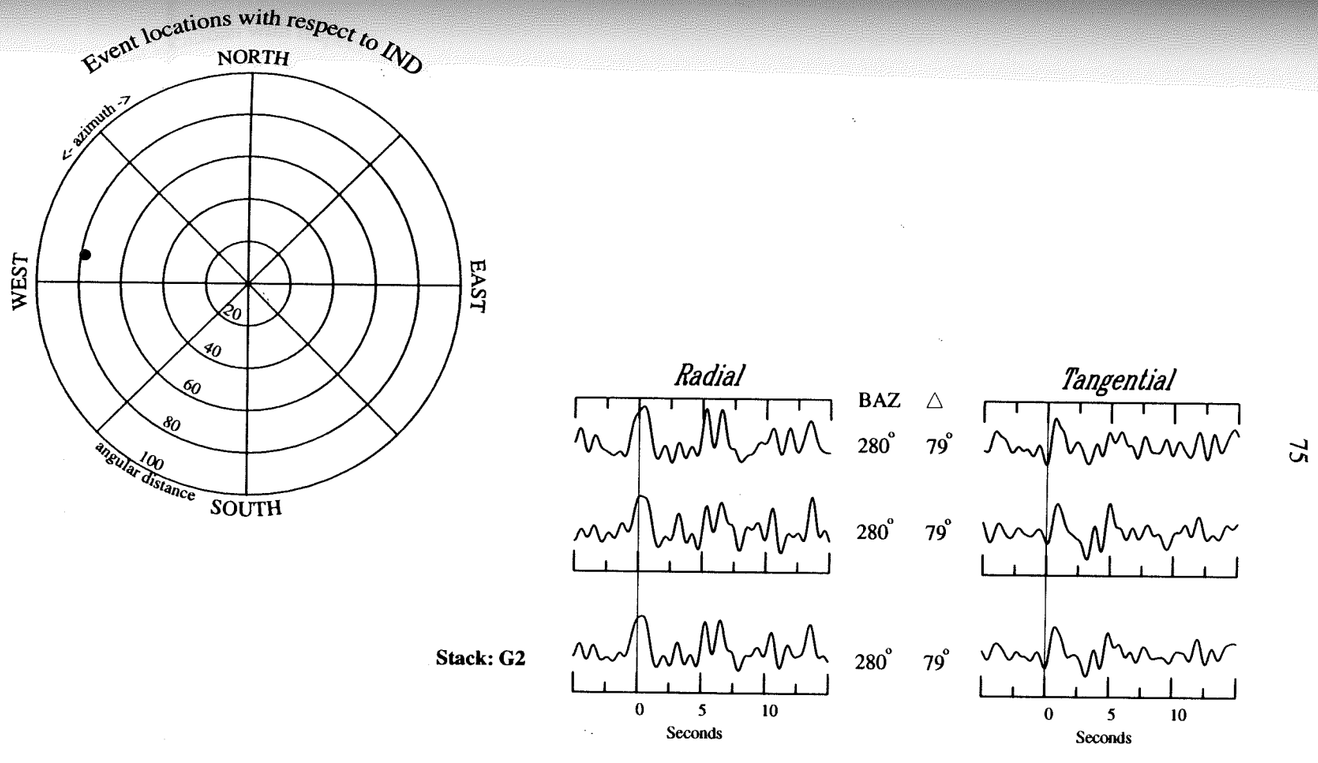

Figure A.13 Event locations with respect to IND, and radial and tangential receiver functions for events in stacking suite G2. Stack backazimuth and distance are averaged from events in the stack.

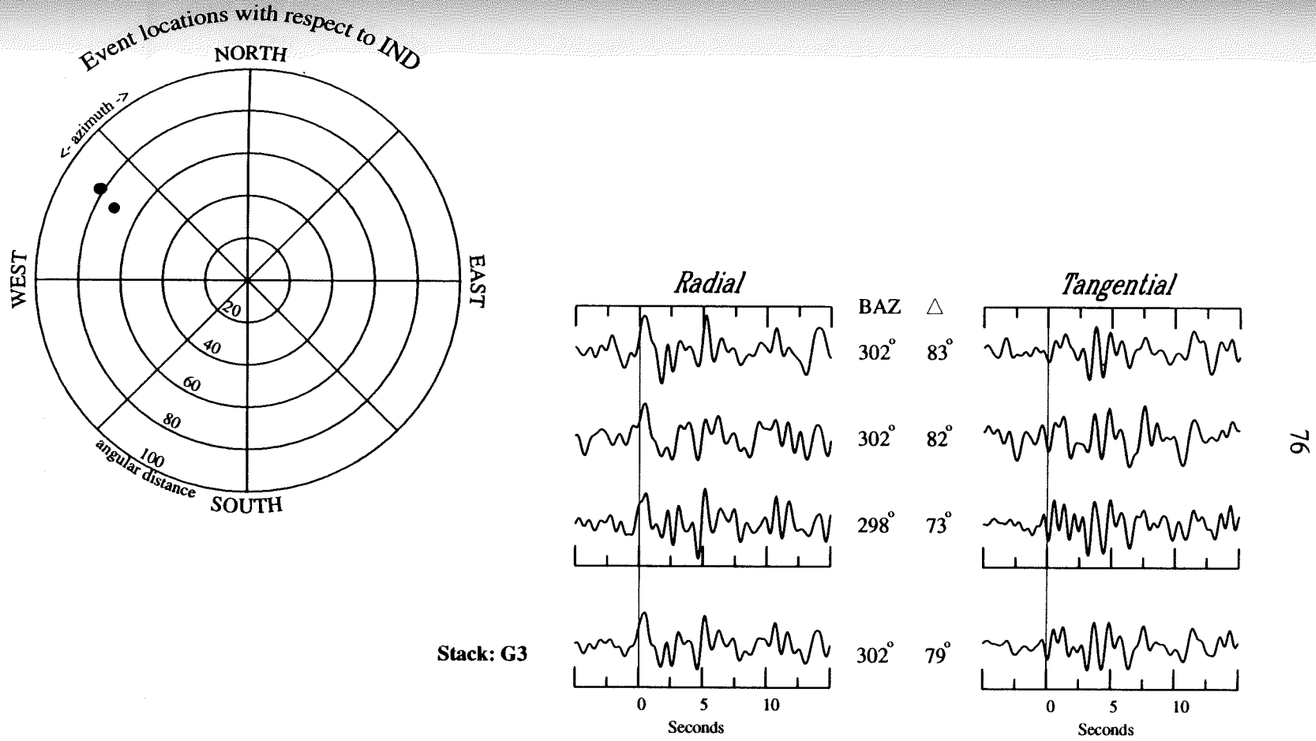

Figure A.14 Event locations with respect to IND, and radial and tangential receiver functions for events in stacking suite G3. Stack backazimuth and distance are averaged from events in the stack.

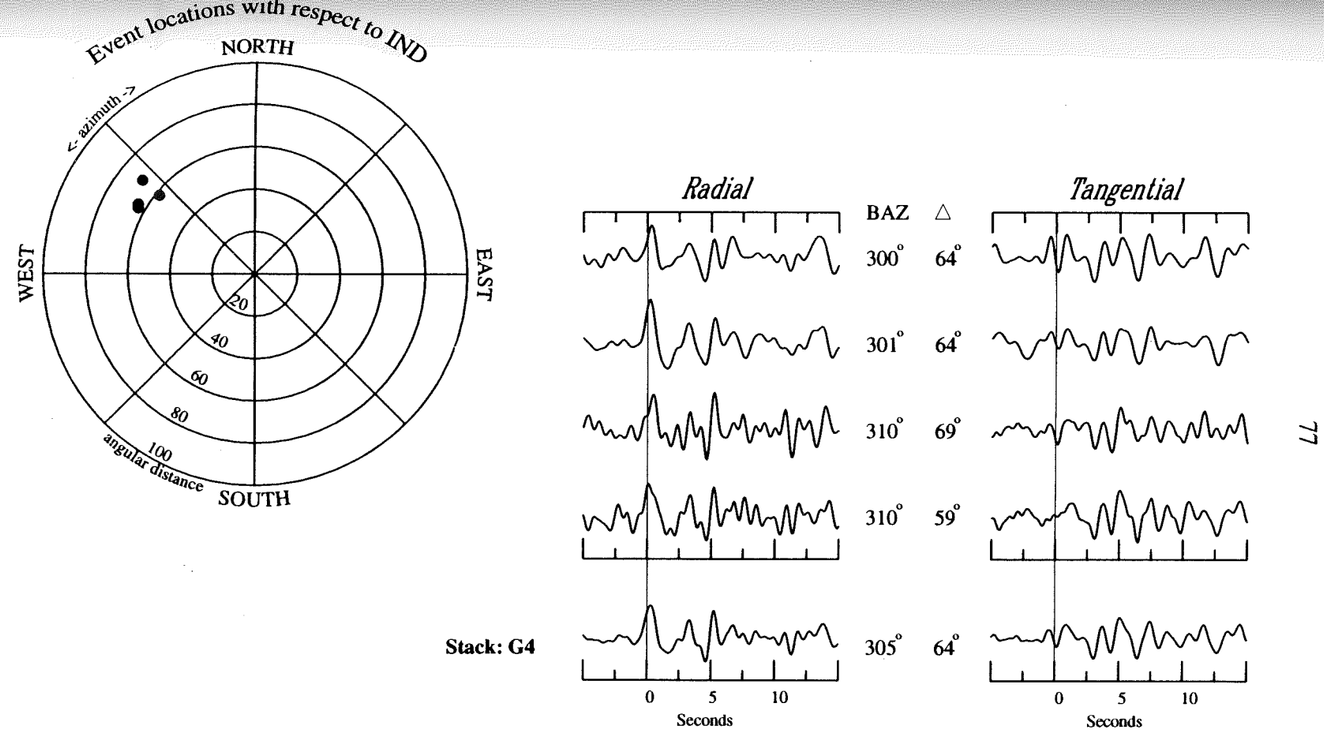

Figure A.15 Event locations with respect to IND, and radial and tangential receiver functions for events in stacking suite G4. Stack backazimuth and distance are averaged from events in the stack.

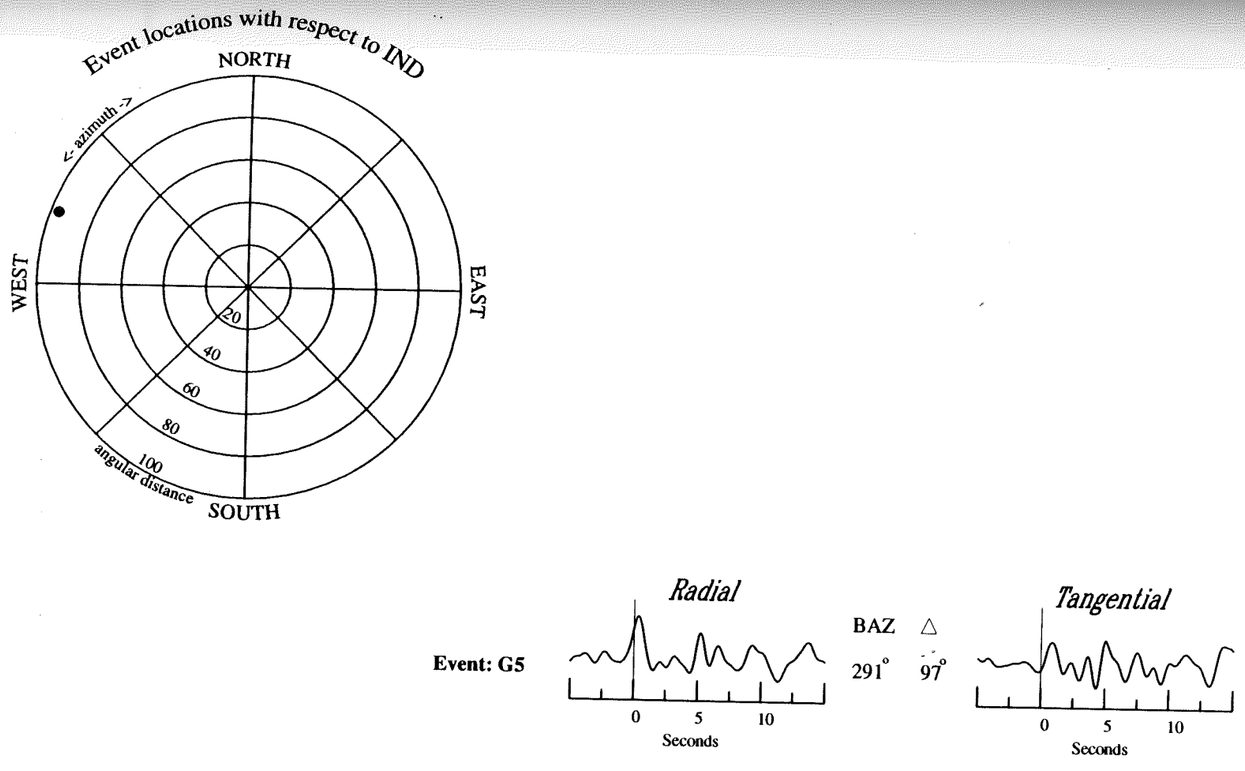

Figure A.16 Event location with respect to IND, and radial and tangential receiver functions for event G5.

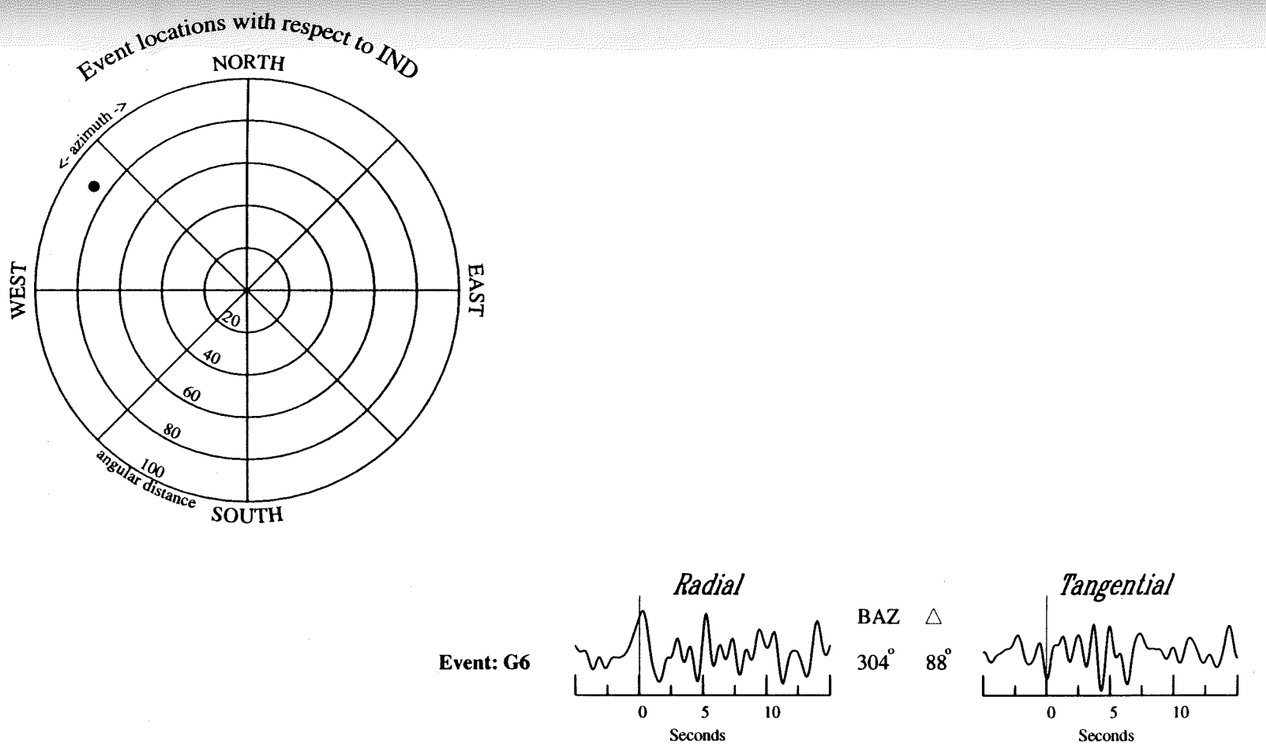

Figure A.17 Event location with respect to IND, and radial and tangential receiver functions for event G6.

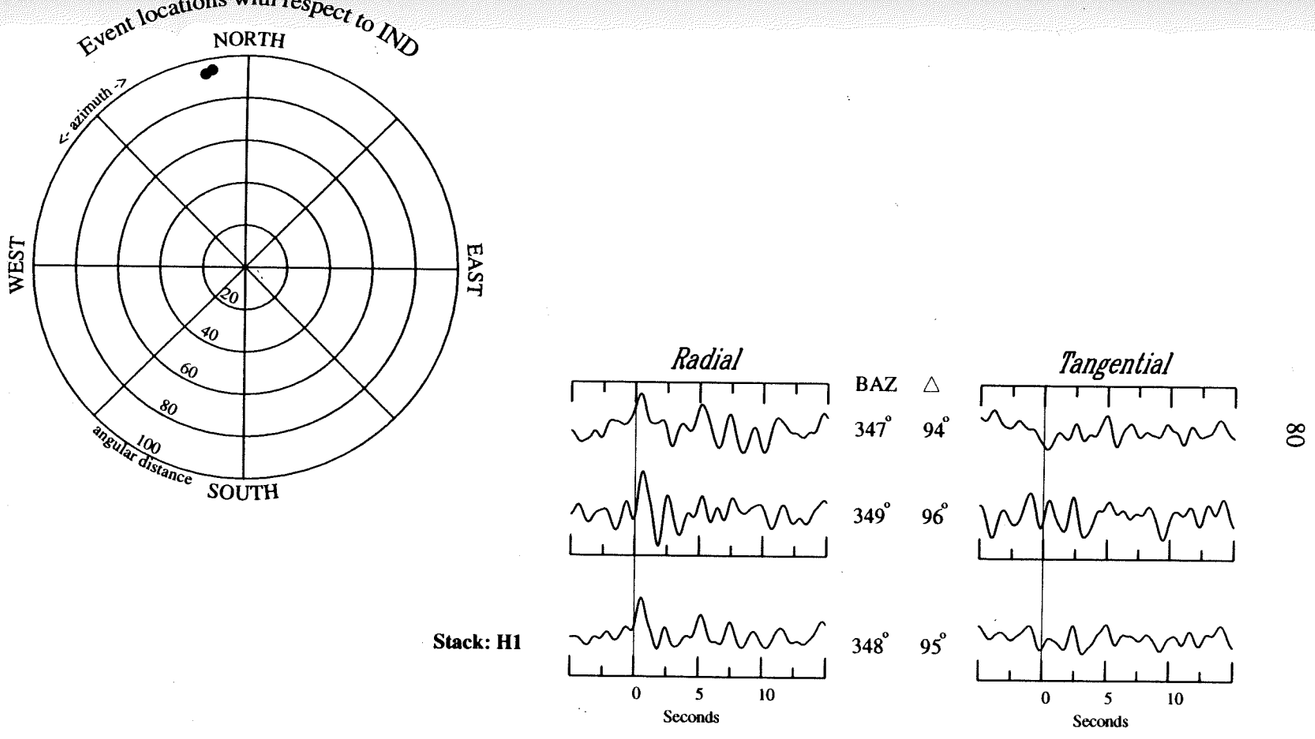

Figure A.18 Event locations with respect to IND, and radial and tangential receiver functions for events in stacking suite H1. Stack backazimuth and distance are averaged from events in the stack.